

JGR Earth Surface

RESEARCH ARTICLE

10.1029/2021JF006132

Key Points:

- Eulerian two-phase simulations identify the importance of wave period in determining the equilibrium ripple geometry
- The importance of the wave period is due to the development time of primary vortices and their resulting length
- The near-bed load is dominant in the growing orbital ripples while the suspended load is conducive to the decaying regime and sheet flows

Supporting Information:

Supporting Information may be found in the online version of this article.

Correspondence to:

A. Salimi-Tarazouj,
alisalim@udel.edu

Citation:

Salimi-Tarazouj, A., Hsu, T.-J., Traykovski, P., & Chauchat, J. (2021). Eulerian two-phase model reveals the importance of wave period in ripple evolution and equilibrium geometry. *Journal of Geophysical Research: Earth Surface*, 126, e2021JF006132. <https://doi.org/10.1029/2021JF006132>

Received 17 FEB 2021

Accepted 19 JUN 2021

Eulerian Two-Phase Model Reveals the Importance of Wave Period in Ripple Evolution and Equilibrium Geometry

Ali Salimi-Tarazouj¹ , Tian-Jian Hsu¹ , Peter Traykovski² , and Julien Chauchat³ 

¹Center for Applied Coastal Research, Civil and Environmental Engineering, University of Delaware, Newark, DE, USA, ²Applied Ocean Physics and Engineering, Woods Hole Oceanographic Institution, Falmouth, MA, USA, ³LEGI, University of Grenoble Alpes, Grenoble, France

Abstract The evolution of ripple geometries and their equilibrium states due to different wave forcing parameters are investigated by a Reynolds-averaged two-phase model, SedFoam, in a two-dimensional domain. Modeled ripple geometries, for a given uniform grain diameter, show a good agreement with ripple predictors that include the wave period effect explicitly, in addition to the wave orbital excursion length (or wave orbital velocity amplitude). Furthermore, using a series of numerical experiments, the ripple's response to a step-change in the wave forcing is studied. The model is capable of simulating “splitting,” “sliding,” “merging,” and “protruding” as the ripples evolve to a new equilibrium state. The model can also simulate the transition to sheet flow in energetic wave conditions and ripple reformation from a nearly flat bed condition. Simulation results reveal that the equilibrium state is such that the “primary” vortices reach half of the ripple length. Furthermore, an analysis of the suspended load and near-bed load ratio in the equilibrium state indicates that in the orbital ripple regime, the near-bed load is dominant while the suspended load is conducive to the ripple decaying regime (suborbital ripples) and sheet flow condition.

Plain Language Summary Seabed sand ripples with a variety of lengths and heights are ubiquitous in the sandy near-shore regions. The complex coupling between flow and sediment transport determines the ripple geometry which affects the energy dissipation of waves and currents, post-storm beach recovery, acoustic sensor operation, and benthic ecosystems. Although many equilibrium-ripple geometry predictors have been developed, there are significant discrepancies among them. Particularly, there is not a consensus on the wave period effect in ripple evolution and equilibrium geometry. In this study, an Eulerian two-phase model for sediment transport applications, SedFoam, is utilized to study the ripple evolution in response to step-changes of the oscillatory flow mimicking the surface waves. The model successfully simulates ripple evolution and resulting equilibrium geometry for different initial bed profiles and combinations of flow period and intensity. Model results explain the importance of the wave period as it determines vortices due to flow separation, which further controls the ripple geometry. Results also confirm the role of near-bed load transport and suspended load transport in the growing and diminishing of sand ripples.

1. Introduction

Orbital motions of surface waves near the seabed can generate various ripples with different geometries, characterized primarily by ripple length and ripple height. The presence of sand ripples is a major cause of bottom friction of waves and currents and it is an essential part of the large-scale hydrodynamic modeling in the coastal ocean. Meanwhile, migrating ripples play an important role in biogeochemical processes as they can retain and bury organic particles (Zlatanović et al., 2017). The migration of sand ripples is also a major form of sediment transport shaping large-scale coastal morphological evolution. The variation of ripple geometry between various wave-formed ripple regimes (orbital ripple, suborbital ripple, and anorbital ripple regimes), or even just limited to the orbital ripple regime, is highly complex (Doucette & O’Donoghue, 2006; Hay & Mudge, 2005; Testik et al., 2005; Traykovski et al., 1999). This complexity is due to the dynamic coupling between hydrodynamics and sediment transport over small-scale topological features. For example, during each flow cycle, the periodic vortex generation-ejection process causes onshore and

offshore sediment fluxes, while the ripple migration rate and net sediment transport rate are due to the subtle balance of these fluxes (Traykovski et al., 1999; van der Werf et al., 2007).

For ripples in equilibrium with a non-variable flow forcing, there has been a long history of developing quantitative predictors for ripple geometry, namely, the ripple length (λ) and the ripple height (η) (or the ripple steepness η/λ) based on the hydrodynamics and sediment characteristics (e.g., Miller & Komar, 1980; Mogridge et al., 1994; O'Donoghue et al., 2006; Pedocchi & García, 2009; Traykovski, 2007; Wiberg & Harris, 1994). Complete reviews of these ripple predictors are provided by Soulsby and Whitehouse (2005) and Nelson et al. (2013). These various methods use different non-dimensional parameters and predict ripple geometry following different strategies. Some predictors distinguish between the ripples formed in the field and the laboratory conditions (Grant & Madsen, 1982; Nielsen, 1981) without identifying the ripple types explicitly. Following the approach developed in Clifton (1976), Wiberg and Harris (1994) provide an iterative predictor using both field and laboratory data. They relate the wave boundary layer thickness (δ_w) to orbital excursion length $d_0 = U_0 T / \pi$ (where U_0 is the orbital velocity and T is the wave period), and then use D_{50} , d_0 and an estimated anorbital ripple height (λ_{ano}) to predict the geometry for all types of vortex ripples. Wiberg and Harris (1994) show that for orbital ripples, the ripple height is larger than the wave boundary layer thickness and they are formed when $d_0/\eta < 10$. On the other hand, anorbital ripples are submerged within the wave boundary layer and they exist when $d_0/\eta > 100$. The suborbital ripples exist as a transition between orbital and anorbital ripples. Malarkey and Davies (2003) provide a non-iterative version of the Wiberg and Harris (1994) predictor solely based on d_0/D_{50} . The model shows that the transition from orbital ripple to suborbital ripple occurs at $d_0/D_{50} = 1,754$, while the transition from suborbital to anorbital ripple occurs at $d_0/D_{50} = 5,587$. At $d_0/D_{50} = 13,020$, the sheet flows prevail. In the Wiberg-Harris type predictor, the ripple geometry depends directly on d_0 , which is the combination of U_0 and T . However, the wave period does not directly control the ripple geometry.

The importance of wave period on the resulting equilibrium ripple geometry, particularly the ripple length, remains a lack of consensus. This is partly because the physical mechanisms explaining the effect of wave period on ripple geometry are not well-understood. Earlier studies, such as Bagnold and Taylor (1946) and Miller and Komar (1980), do not include wave period to explain ripple geometry. To our knowledge, the role of the wave period on ripple formation and evolution is first considered by Mogridge and Kamphuis (1972). Later, Mogridge et al. (1994) refine the formulation by explicitly including the period parameter calculated as $\chi = D_{50}/(s - 1)gT^2$ along with d_0/D_{50} . For a given period parameter (χ), Mogridge et al. (1994) observe the growth of ripples to a maximum possible length and height (λ_m , η_m) by increasing the velocity amplitude (U_0) (hence d_0). The corresponding velocity amplitude (U_{0m}) and orbital excursion length, d_{0m} are then readily defined. Throughout this “growing regime”, the ripple length is proportional to orbital excursion length with a proportional constant between 0.65–1.0, depending on the period parameter. However, Mogridge et al. (1994) predict a constant ripple length after increasing the orbital excursion length beyond d_{0m} , which is inconsistent with field observations. Field data reported by Nielsen (1981) indicates the existence of a “decay regime” of the ripple length when $d_0 > d_{0m}$. Instead of using two independent parameters of χ and d_0 / D_{50} , Nielsen (1981) combine these two parameters into the mobility number as $\psi = (\pi d_0 / T)^2 / (s - 1)gD_{50}$ and provide two sets of single-parameter expressions for laboratory and field conditions.

Extensive one-month field observations in a coarse sand continental shelf ($D_{50} = 0.4$ mm, and water depth $h = 11$ m) by Traykovski et al. (1999) demonstrate that ripples under long-period waves ($T = 10$ –15 s) reach a longer length than that predicted by Wiberg and Harris (1994) before transitioning to suborbital (decaying) regime. By using the mobility-number-based ripple predictor of Nielsen (1981) and Traykovski et al. (1999) show that for $T \approx 15$ s, λ_m is observed to occur at $d_0 / D_{50} = 3,250$, suggesting that the transition from orbital to sub-orbital ripple is at a significantly larger d_0 / D_{50} value than the $d_0 / D_{50} = 1,754$ suggested by Wiberg and Harris (1994) (or by Malarkey and Davies [2003]). O'Donoghue and Clubb (2001) and O'Donoghue et al. (2006) compare the above-mentioned ripple predictors for their predicted d_{0m} and λ_m (or more generally, it can be interpreted as the demarcation between orbital to suborbital ripples). For the Wiberg and Harris (1994) predictor, the maximum ripple length only depends on sediment size ($d_{0m} / D_{50} = 1,754$), independent of wave period (or χ), and the corresponding $\lambda_m = 0.62d_{0m}$. On the other hand, for both Nielsen (1981) and Mogridge et al. (1994) predictors, d_{0m} and λ_m change with respect to χ and higher values of

d_{0m} and λ_m are obtained in typical field-scale flows with longer periods (at $\chi = O(10^{-7})$), consistent with field observations reported by Traykovski et al. (1999). O'Donoghue and Clubb (2001) also confirm that several models predict approximately the same d_{0m} for laboratory-scale flow conditions at $\chi = O(10^{-6})$. For a given D_{50} and T , O'Donoghue and Clubb (2001) (see Figure 2 of their paper) summarizes that when d_0 is smaller than d_{0m} the ripple is in the “growing regime” and the ripple length is proportional to the orbital length ($\lambda = \beta d_0$), similar to the previously defined “orbital ripples,” but with β depending on wave period. By increasing d_0 beyond d_{0m} , the ripple length decays and eventually becomes sheet flow. Generally, the wave period effect should be included explicitly in predicting ripple geometry to cover both laboratory- and field-scale wave conditions. Later, O'Donoghue et al. (2006) further revised the Nielsen (1981) formula to improve the predicted rapid fall-off in ripple steepness at high mobility numbers.

Most of the aforementioned laboratory studies focus on the equilibrium ripple geometry subjected to a constant oscillatory flow forcing. The flow characteristics in the coastal environment, however, can change significantly due to a storm passage (Crawford & Hay, 2001; Hay & Mudge, 2005; Traykovski et al., 1999). Changes in the wave conditions (i.e., T and U_0 or d_0) can cause the growth, deformation and disappearance of the existing ripples. During the growing of a storm, Traykovski et al. (1999) observe an increase of ripple length in a coarse sand ($D_{50} = 0.4$ mm) environment as the orbital excursion length increases, while under the waning flows, ripples evolve into smaller sizes. The observations conducted by Crawford and Hay (2001) in a nearshore sandy beach with finer sand ($D_{50} = 0.174$ mm) showed the formation and migration of the “Linear Transition Ripples” (LTRs) during the growth and decay phase of a storm. They are long-crested, low-steepness anorbital ripples, observed at a wave energy condition just below the transition to sheet flow. Hay and Mudge (2005) reported observation in a similar environment showing five different bed states including irregular ripples, cross ripples, LRTs, mega-ripples, and flat-bed. Although the growth and decay of ripples associated with wave energy are similar to the coarse sand environment reported by Traykovski et al. (1999), the specific ripple type in the fine sand environment, such as the existence of LRTs, mega-ripple, and 3D ripples, are different. The observed dependence on grain size may be due to different contributions of suspended load and near-bed load.

Besides the field observations, laboratory studies have been reported to better quantify the ripple evolution process in well-controlled conditions. For instance, the sand tray experiment conducted by Hansen, van Hecke, Ellegaard, Andersen, Bohr, and Sams (2001) shows that by keeping the same oscillatory period T while decreasing the orbital velocity amplitude U_0 (consequently, d_0) sufficiently, the ripple “doubling” process takes place through the generation of the secondary crest in-between the original ripple marks. On the contrary, increasing the orbital excursion length for a fixed oscillatory period results in larger length ripples via “bulging”. Wave flume experiments have also been carried out to study ripple evolution (e.g., Sekiguchi & Sunamura, 2004; Testik et al., 2005). By keeping a constant wave period while changing the wave orbital excursion length in a laboratory wave flume, Testik et al. (2005) show that ripple adjustment to a new wave condition occurs through “splitting,” “flattening,” and “regrowth.” By decreasing the orbital excursion length moderately, the ripple “splitting” occurs, which is similar to the doubling process reported by Hansen, van Hecke, Ellegaard, Andersen, Bohr, and Sams (2001). However, by significantly decreasing the orbital excursion length, the ripple crest “flattening” occurs, in which the trough became more angular, similar to the “inversed” ripples observed by Evans (1943). Moreover, an increase in orbital excursion length results in the regrowth of ripples into a longer length. Doucette and O'Donoghue (2006) carry out full-scale oscillatory water tunnel experiments to study the response of orbital ripples, consisting of sand grain size $D_{50} = 0.44$ mm, subjected to changes in the oscillatory flows. They observe the evolution of orbital ripples from a flat bed, or a bed that consists of very small ripples, to occur through “sliding” and “merging”. “Sliding” refers to the increase or decrease of ripple length through the movement of the ripple's crest toward or away from each other. “Merging” describes the process in which a ripple attenuates in height and merges into the adjacent ripples causing the growth of ripple length similar to the regrowth process reported by Testik et al (2005). Doucette and O'Donoghue (2006) also observe the evolution of large ripples to smaller ripples occurs through combined “splitting” and “merging”. The final equilibrium ripple geometry is independent of the initial ripple bed morphology while the time required to reach the equilibrium depends on the flow intensity, which can be quantified by the mobility number. Hansen, van Hecke, Ellegaard, Andersen, Bohr, Haaning, and Sams (2001) report unique 3D ripple pattern, called bulging defects, in the ripple evolution, which are spatulated to be driven by Rayleigh-Plateau instabilities. Perron et al. (2018) report

similar deviation from straight and evenly spaced ripple pattern and emphasize their importance in the rock record. Both Doucette and O'Donoghue (2006) and Testik et al. (2005) do not report the bulging defects perhaps due to their limited domain width in the spanwise direction.

Over the past few decades, a variety of numerical modeling approaches has been applied to investigate the vortices and turbulent flow characteristics over fixed ripples driven by oscillatory flows, including the inviscid discrete vortex method (Longuet-Higgins, 1981), Lattice Boltzmann method (Nienhuis et al., 2014), Reynolds-averaged Navier-Stokes (RANS) models (e.g., Chang & Hanes, 2004; van der Werf et al., 2008), Large-eddy simulations (LES, Chang & Scotti, 2003; Dimas & Leftheriotis, 2019; Harris & Grilli, 2014; Zedler & Street, 2006) in high Reynolds number conditions, and Direct Numerical Simulations (DNS, Blondeaux & Vittori, 1991; Önder & Yuan, 2019; Scandura et al., 2000) for low to moderate Reynold numbers. These fixed-ripple numerical studies reveal insight into the periodic formation, ejection, and dissipation of vortices over bedforms, however, the dynamic coupling between the hydrodynamics, sediment transport, and small-scale morphological evolution is neglected. Marieu et al. (2008) and Chou and Fringer (2010) utilize RANS and LES for turbulent flows, coupled with the conventional suspended load and bedload formulations for sediment transport, to simulate ripple evolutions and migrations with promising results. However, these types of approaches require empirical formulae for reference concentration, bedload transport rate, and avalanche scheme. As these formulations are mainly developed for turbulence-averaged flows, their adoption in turbulence-resolving LES may lead to an overestimation of ripple evolution speed (Chou & Fringer, 2010).

To model the full profile of sediment transport and avoid using the bedload/suspended load assumptions to simulate ripple evolution, different approaches have been taken. Penko et al. (2011, 2013) apply a 3D mixture model to study ripple evolution in which the sediment-fluid mixture is treated as a single continuum. By using the Reynolds-Averaged Eulerian two-phase equations for fluid and sediment phases, Salimi-Tarazouj et al. (2021) successfully simulate onshore ripple migration forced by a Stokes second-order oscillatory flow reported in the laboratory experiment of van der Werf et al. (2007). The model can reproduce the asymmetric vortex field over the ripple driven by the onshore-skewed oscillatory flow. Model results are used to quantify the relative contributions from the near-bed load and suspended load, which reveal that besides the primary vortex generation-ejection process pertinent for a net offshore-directed suspended sediment flux, the speedup of the boundary layer flow over the stoss side of the ripple bed, which is further enhanced by the returning flow of the primary vortex, and the avalanching at the lee side of the ripple, all contribute to the net onshore directed near-bed sediment flux. However, when driven by a symmetric (sinusoidal) oscillatory flow, the suspended and the near-bed sediment fluxes are completely symmetric and the net transport rate and ripple migration rate are zero. This dynamic coupling between the hydrodynamics and the sediment transport not only determines the ripple migration, but also forces the ripple formation, geometrical evolution, and annihilation. The present study continues the work of Salimi-Tarazouj et al. (2021) and focuses on the latter.

The Eulerian two-phase model SedFoam (Chauchat et al., 2017; Cheng et al., 2017; Salimi-Tarazouj et al., 2021) is utilized to study ripple evolutions in this paper with two scientific objectives: (1) To study the effect of wave period on the equilibrium ripple geometry, and meanwhile, the numerical model is verified by several existing ripple predictors. (2) To study ripple response to a step-change in the wave orbital motion for several different scenarios in order to elucidate the key factors controlling the transient process. Analysis of these different scenarios allows us to relate the varying degree of suspended load flux versus the near-bed load flux to the resulting ripple evolution. The remaining of the paper is organized as follows. The model formulation is presented in Section 2, and Section 3 is dedicated to the model setup. The model results are presented in Section 4. Concluding remarks are provided in Section 5.

2. Methods

2.1. Numerical Model

The Eulerian two-phase model SedFoam is an open-source model (Chauchat et al., 2017; Cheng et al., 2017) developed using the OpenFOAM Computational fluid dynamics toolbox (version 2.4.0, Weller et al., 1998). Unlike the single-phase model for sediment transport modeling, the two-phase model can resolve the full

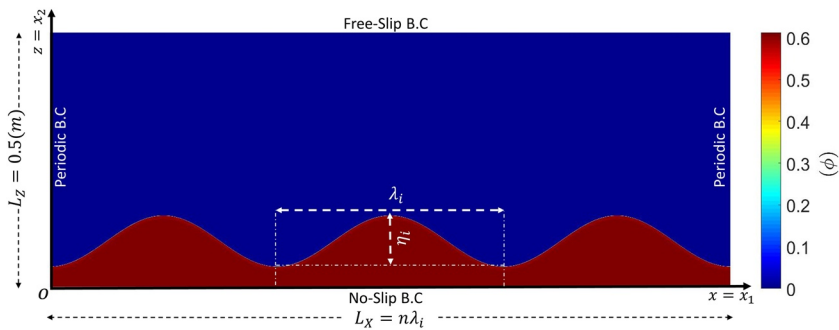


Figure 1. Schematic plot of model domain and initial ripple bed. The color bar shows the sediment volumetric concentration.

profiles of fluid velocities, sediment velocities, sediment concentration, and fluid pressure from the porous ripple bed to the dilute sediment transport without artificially separating sediment transport into the bedload layer and the suspended load layer. By resolving the full profiles, the evolution of ripple bed is directly solved by the Eulerian two-phase mass and momentum equation (see Equations 1 and 2) without the need to use the Exner equation. Recently, Salimi-Tarazouj et al. (2021) validate SedFoam using the Reynolds-averaged formulation with measured flow velocity, sediment concentration, and ripple migration data reported by van der Werf et al. (2007). In this study, we adopt the same Reynolds-averaged formulation, and the two-dimensional-vertical (2DV) model domain which is depicted in Figure 1. The oscillatory flow is generated in the streamwise (x) direction. The ripples are assumed to be homogeneous in the spanwise (y) direction and the model describes the turbulence-averaged flow in the xz -plane. The general model formulation, including different choices of turbulence closure, and shear-induced particle stress closures, are documented in detail in Chauchat et al. (2017). For the specific model formulation to simulate ripple dynamics, including the $k-\epsilon$ closure for flow turbulence and the kinetic theory of granular flow for shear-induced particle stress, the readers are referred to Salimi-Tarazouj et al. (2021) for a comprehensive discussion. Here, we briefly discuss the key model elements in the Reynolds-averaged Eulerian two-phase formulation that allows the model to resolve the full profile of sediment transport processes.

In the Eulerian two-phase formulation, the carrier fluid (water) and dispersed particles (sand assumed to be of uniform properties) are governed by their individual mass and momentum equations. The Reynolds-averaged mass conservation equations for fluid and sediment phases are written as:

$$\frac{\partial(1-\phi)}{\partial t} + \frac{\partial(1-\phi)u_i^f}{\partial x_i} = 0 \quad (1)$$

and

$$\frac{\partial\phi}{\partial t} + \frac{\partial\phi u_i^s}{\partial x_i} = 0 \quad (2)$$

where u_i^f and u_i^s represents fluid and sediment phase velocities, respectively, and tensor notation with the subscript i (or j) = 1, 2 is used to represent streamwise (x) and vertical (z) directions. Sediment volumetric concentration is expressed by ϕ . The momentum equations for fluid and sediment phases are written as

$$\frac{\partial\rho^f(1-\phi)u_i^f}{\partial t} + \frac{\partial\rho^f(1-\phi)u_i^fu_j^f}{\partial x_j} = -(1-\phi)\frac{\partial P^f}{\partial x_i} + (1-\phi)f_i + \frac{\partial\tau_{ij}^f}{\partial x_j} - \rho^f(1-\phi)g\delta_{i2} + M_i^{fs} \quad (3)$$

and

$$\frac{\partial\rho^s\phi u_i^s}{\partial t} + \frac{\partial\rho^s\phi u_i^su_j^s}{\partial x_j} = -\phi\frac{\partial P^f}{\partial x_i} + \phi f_i - \frac{\partial P^s}{\partial x_i} + \frac{\partial\tau_{ij}^s}{\partial x_j} - \rho^s\phi g\delta_{i2} + M_i^{sf} \quad (4)$$

where P^f is the fluid pressure, $\rho^f = 1,000\left(\text{kg/m}^3\right)$ and $\rho^s = 2,650\left(\text{kg/m}^3\right)$ are water and sand grain density, respectively, and $g = 9.81\left(\text{m/s}^2\right)$ is the gravitational acceleration. The external pressure gradient that drives the flow is represented by f_i and its explicit form will be discussed later. The fluid stress τ_{ij}^f includes the grain-scale stress and turbulent Reynolds stress. The former is of minor importance in the present turbulent flow applications and it is simply modeled as viscous stress with the fluid molecular viscosity $\nu^f = 10^{-6}\left(\text{m}^2/\text{s}\right)$, while the latter is modeled by the turbulent eddy viscosity ν^{ft} with a k - ε closure model. In two-phase flow formulation, a unique term is the momentum transfer between the fluid phase and sediment phase expressed as M_i^{fs} and M_i^{sf} , and following Newton's third law, it requires $M_i^{fs} = -M_i^{sf}$. The momentum exchange in this study is modeled as (Salimi-Tarazouj et al., 2021):

$$M_i^{fs} = -\phi\beta(u_i^f - u_i^s) + \beta\frac{\nu^{ft}}{\sigma_c}\frac{\partial\phi}{\partial x_i} \quad (5)$$

The two terms on the right-hand-side (RHS) model the drag force with β as the drag parameter. Specifically, the first term represents the averaged drag force proportional to the Reynolds-averaged velocity difference between fluid and particle phases. The second term has resulted from the correlation of turbulent fluctuations between the sediment concentration and fluid velocity. The gradient transport assumption is adopted here and the Schmidt number $\sigma_c = 1$ is specified for simplicity. This term represents the well-known turbulent suspension/diffusion of sediment. The drag parameter β models the linear and nonlinear drag law for a sphere with the hindered settling effect.

The closures of particle pressure (P^s) and particle shear stress (τ_{ij}^s) control the transition from fluid-like to solid-like behavior of sediment bed and they are instrumental to model near-bed load and ripple evolution. Model results are generally sensitive to these closures. In dilute and moderate concentration, particle stresses are generated by high flow shear via particle collisions. However, when sediment concentration is higher than the random-loose packing (ϕ_c) threshold, particle stress is mainly caused by enduring contact as the flow shear diminishes. In the present model, particle pressure (P^s) and particle shear stress (τ_{ij}^s) are assumed to consist of a collisional component (superscript "sc") and an elastic/frictional contact component (superscript "sf"):

$$P^s = P^{sc} + P^{sf} \quad (6)$$

$$\tau_{ij}^s = \tau_{ij}^{sc} + \tau_{ij}^{sf} \quad (7)$$

We adopt the kinetic theory of granular flow for the collisional components based on the granular temperature (defined as one-third of kinetic energy of particle velocity fluctuation). The particle pressure due to elastic/frictional contact in the highly concentrated region is calculated following Johnson et al. (1990) to model the elastic behavior of the sediment bed:

$$P^{sf} = \begin{cases} 0, & \phi_c < 0.57 \\ 0.05 \frac{(\phi - 0.57)^3}{(0.635 - \phi)^5}, & \phi_c \geq 0.57 \end{cases} \quad (8)$$

The particle shear stress in the highly concentrated quasi-static (nearly zero shear rate) region is modeled as,

$$\tau_{ij}^{sf} = 2\rho^s\nu_{Fr}^s S_{ij}^s \quad (9)$$

where ν_{Fr}^s is the frictional viscosity and S_{ij}^s is the deviatoric part of the sediment phase strain rate. A friction viscosity is readily calculated by relating the particle pressure and particle shear stress by a frictional angle θ_f (Schaeffer, 1987),

$$v_{Fr}^s = \frac{P^{sf} \sin(\theta_f)}{\rho^s \left(|S_{ij}^s|^2 + D_{\text{small}}^2 \right)^{1/2}}. \quad (10)$$

According to Salimi-Tarazouj et al. (2021), θ_f controls the threshold angle of the resolved avalanching process during ripple migration and it is specified as $\theta_f = 32^\circ$ similar to the angle of repose for cohesionless sand grains. To ensure the numerical stability when the shear rate approaches zero in very high sediment concentration close to the immobile bed, regularization technique (Chauchat & Médale, 2014) is used and $D_{\text{small}} = 10e - 10$ is specified. For all the cases presented in this study, sediment phase stress closures and corresponding coefficients and parameters are kept the same as those used in Salimi-Tarazouj et al. (2021). Detailed expressions for the drag parameter β , k - ϵ turbulence closure model and the collisional and frictional component of the particle stress can be found in Salimi-Tarazouj et al. (2021). More detailed information on main model input parameters, including k - ϵ turbulence coefficients and sediment stress closures are also provided in the supporting information.

To resolve the ripple evolution dynamics, a stable and immobile rippled bed needs to be established as the initial condition while the initial fluid and particle velocities are set to be zero. Following Salimi-Tarazouj et al. (2021), the sediment concentration profile obtained from a one-dimensional vertical simulation, after the flow reaching the equilibrium (Cheng et al., 2017) is mapped to every vertical (z -direction) grid column throughout the entire streamwise (x) direction in the model domain with the vertical location of each profile adjusted by the prescribed initial sinusoidal bathymetry (see Figure 1). This mapping procedure is required in order to establish appropriate initial contact stresses $P^{sf} = f(\phi)$ and $\tau^{sf} = f(P^{sf})$ (see Equations 8–10) in the ripple bed and prevent unrealistic initial slumping.

Figure 1 shows a schematic plot of the model domain. At the top boundary, a free-slip (i.e., Neumann) boundary condition is used for both the fluid and sediment phase quantities. For the pressure field, a fixed zero value is specified at the top boundary. At the bottom of the model domain, a no-slip boundary condition is applied for the velocities of both phases while a zero-gradient boundary condition is specified for other quantities. It is reminded that in the present two-phase model, the whole profiles of primary variables throughout the water column down to the immobile bed are resolved, and the no-slip boundary at the bottom of the model domain plays a minor role in the results because it is under a sufficiently thick layer of immobile sediment bed. To minimize computational domain length, periodic boundary conditions are specified at the two lateral boundaries. As investigated in Salimi-Tarazouj et al. (2021), the imposed periodic boundary condition at two lateral boundaries may limit the growth of ripple length. Therefore, the rationale for the selection of domain length for a given wave condition will be discussed later.

In this study, seven different simulations for ripple geometry evolution are carried out (see Table 2). The oscillatory flow is driven by a prescribed horizontal pressure gradient f_i which generates a free-stream velocity time series following a sinusoidal motion

$$U_0(t) = U_m \sin(\omega t) \quad (11)$$

where U_m is the orbital velocity amplitude and $\omega = 2\pi / T$ is the angular frequency. Modeled grain diameter is specified as coarse sand with $D = 0.44$ mm for all the simulations. Case 1, which has been reported in Salimi-Tarazouj et al. (2021), is designed to model the experiment Mr5b50 of van der Werf et al. (2007) with $U_m = 0.48$ m/s and $T = 5$ s. In this case, we prescribe the initial bed with 3 ripples and hence the domain length is specified as $L_x = 3\lambda_i$ (see Figure 1). The initial ripple length (λ_i) is set to be the same as the measured equilibrium length $\lambda_e = 0.46$ m and we obtain $L_x = 3\lambda_e = 1.38$ m. The initial ripple height is set to be $\eta_i = 0.12$ m, which is significantly larger than the measured equilibrium ripple height of $\eta_e = 0.08$ m and the model's capability to predict ripple height and shape has been validated (Salimi-Tarazouj et al., 2021). The computational domain is discretized into $N_x = 2,400$ uniform grids in the streamwise direction with a grid length $\Delta x \approx 0.55$ mm. The same domain length and mesh discretization are used in other cases. Although the ripple length is expected to increase or decrease as the wave condition changes, the choice of wave conditions in other cases are guided by ripple predictors (see Section 2.2) such that the domain

should approximately consist of the multiples of the expected ripple length. The domain height is set to be $L_z = 0.5$ m in all the simulations. By examining the simulated velocity profile, we confirmed that this domain height is sufficiently large to cover the wave bottom boundary layer over the ripples. In the vertical direction, $N_z = 438$ non-uniform grid is used. By keeping the grid ratio near unity, $\Delta z \approx 0.5$ mm is used in the lower 0.15 m of the domain where a significant sediment transport takes place and the vertical grid height is gradually increased away from the ripple bed to $\Delta z \approx 3$ mm at the top boundary. The initial ripple bed in Case 2a is specified to be the same as that of Case 1. However, the final bed profile of Case 1 is used as the initial ripple bed for Case 2b, Case 3, and Case 5. Moreover, the final bed profiles obtained in Case 3 and Case 5 are used as the initial ripple bed for simulating Case 4 and Case 6, respectively (see Table 2). The design of these simulations allows us to investigate how different oscillatory flow forcings and the initial ripple beds evolve to different (or the same) equilibrium states.

In this study, the ripple's surface is defined as the volumetric concentration $\phi = 0.57$ and the ripple crest and trough are determined by identifying the highest and the lowest point of the ripple profile. The modeled ripple length can be determined from the horizontal distance between two adjacent crests and the ripple height is defined as the vertical distance between the crest and the trough. Consistent with the periodic boundary condition specified at the two lateral boundaries, the modeled ripple length and height are obtained by averaging crest-to-crest and trough-to-crest distances of all the ripples in the domain, respectively.

2.2. Empirical Ripple Predictors

A major goal of this study is to investigate the effect of wave period T on the ripple equilibrium geometry while verifying the model's predictive capability with several existing ripple predictors. Several empirical ripple predictors that will be used for this investigation are summarized here.

The non-iterative version of Wiberg and Harris (1994) predictor is provided by Malarkey and Davies (2003). The ripple length is calculated based on the ratio of orbital excursion length to mean grain diameter d_0 / D_{50} for three ripple regimes:

$$\begin{cases} \lambda_{\text{orb}} = 0.62d_0 & \frac{d_0}{D_{50}} < 1754 \\ \lambda_{\text{sub}} = \lambda_{\text{ano}} e^{f\left(\frac{d_0}{\lambda_{\text{ano}}}\right)} & 1754 \leq \frac{d_0}{D_{50}} \leq 5587 \\ \lambda_{\text{ano}} = 535D_{50} & \frac{d_0}{D_{50}} \geq 5587 \end{cases} \quad (12)$$

with $f\left(d_0 / \lambda_{\text{ano}}\right) = -\ln\left(\lambda_{\text{orb}} / \lambda_{\text{ano}}\right) \ln\left(0.01 d_0 / \lambda_{\text{ano}}\right) / \ln(5)$. After calculating the ripple length using Equation 12 and obtaining the (d_0 / λ) , the ripple height η can be obtained as follows,

$$\frac{d_0}{\eta} = \exp\left[B_2 - \sqrt{B_3 - B_1 \ln\left(\frac{d_0}{\lambda}\right)}\right] \quad (13)$$

where $B_1 = 10.52$, $B_2 = 7.59$, and $B_3 = 33.6$ are empirical coefficients. Importantly, the ripple steepness (η / λ) can be calculated from Equations 12 and 13, which is a constant for orbital ripples with $\eta / \lambda = 0.17$ (if $d_0 / D_{50} < 1,754$) and the ripple steepness decays for suborbital and anorbital ripple regimes.

The empirical formula of Nielsen (1981) predicts the ripple length λ based on the mobility number ψ . In this study, we use the Nielsen (1981) formula calibrated for laboratory condition:

$$\lambda / a_0 = 2.2 - 0.345\psi^{0.34}, \quad (14)$$

The ripple steepness η / λ is predicted using the Shields parameter $\theta = 1 / 2f_w\psi$ where the wave friction factor is calculated following the Swart (1974) formula as,

$$f_w = \exp \left[5.213 \left(\frac{2.5D_{50}}{a_0} \right)^{0.194} - 5.977 \right] \quad (15)$$

where $a_0 = d_0 / 2$ represents the orbital excursion amplitude. The ripple steepness is then calculated as

$$\eta / \lambda = 0.182 - 0.24\theta^{1.5}. \quad (16)$$

Because both the mobility number and wave orbital amplitude are functions of wave period, one can rearrange the Nielsen (1981) formulation and obtain a set of curves to relate λ / D_{50} and d_0 / D_{50} for different wave periods and show that the transition from orbital ripple regime (the growing regime) to suborbital ripple regime is a function of the wave period (e.g., Traykovski et al., 1999). On the other hand, the Wiberg and Harris (1994) predictor determines this transition to occur at $d_0 / D_{50} = 1,754$, independent of the wave period. Both Nielsen (1981) and Wiberg and Harris (1994) predict a decay in the ripple length and steepness in the suborbital and anorbital regimes (the decaying regime).

The Mogridge et al. (1994) predictor uses d_0 / D_{50} and the period parameter, χ , to predict the ripple geometry. For the given D_{50} and T , the ripple length in the growing regime is calculated as proportional to d_0 using a function $f_1(\chi)$ that explicitly depends on the period parameter as,

$$\lambda = f_1(\chi) \frac{d_0}{2} \quad (17)$$

where $0.65 < f_1(\chi) = 1.07\chi^{0.05} < 1$. By increasing the d_0 for a fixed period parameter, χ (achieved by increasing the orbital velocity amplitude while keeping the wave period constant) the ripple length can reach a maximum value λ_m at the corresponding orbital excursion length d_{0m} . According to the measured data, the maximum ripple length λ_m is calculated by,

$$\log_{10}(\lambda_m / D_{50}) = 4.032 - 9.089\chi^{0.16422}, \quad (18)$$

and the corresponding excursion length is then calculated as $d_{0m} = 2\lambda_m / f_1(\chi)$. Due to the limitation of their oscillatory flow tunnel preventing high velocities (high mobility number), Mogridge et al. (1994) does not observe a decay in ripple length when d_0 is beyond d_{0m} . In the Mogridge et al. (1994) predictor, the decay of the ripple steepness occurs due solely to the decrease of the ripple height after reaching a maximum value η_m , which is calculated as

$$\log_{10}(\eta_m / D_{50}) = 2.861 - 17.715\chi^{0.2486} \quad (19)$$

Mogridge et al. (1994) provides curves, normalized by λ_m and η_m to predict the ripple length λ and height η for the given period parameter.

To show the difference between these methods, O'Donoghue and Clubb (2001) rearranges the above-mentioned predictors to obtain the orbital excursion length d_{0m} corresponding to the maximum ripple length as

$$\text{Wiberg and Harris: } \frac{d_{0m}}{D_{50}} = 1,754 \quad (20)$$

$$\text{Nielsen: } \frac{d_{0m}}{D_{50}} = 2.26\chi^{-0.5} \quad (21)$$

$$\text{Mogridge et al.: } \frac{d_{0m}}{D_{50}} = 10^{\left(13.4 - 13.8\chi^{0.0205}\right)} \left[\frac{1}{1.07\chi^{0.05}} + 2 \tan \left(\frac{\tan^{-1}(1.07\chi^{0.05})}{2} \right) \right] \quad (22)$$

Table 1

A Summary of the Flow Condition of Each Case was Simulated in This Study

Case ID	T (s)	U_m (m/s)	d_0 (m)	d_0 / D_{50}	ψ Nielsen	θ Shields	$\chi (10^{-6})$ Mogridge	Regime
Case 1	5	0.48	0.76	1,727	32	0.22	1.08	Orbital
Case 2a	3	0.80	0.76	1,727	90	0.6	3.02	Sub-Orbital
Case 2b	3	0.8	0.76	1,727	90	0.6	3.02	Sub-Orbital
Case 3	3	0.48	0.46	1,040	32	0.26	3.02	Orbital
Case 4	3	0.80	0.76	1,727	90	0.6	3.02	Sub-Orbital
Case 5	5	1.5	3.14	5,435	316	1.53	1.08	Sheet-Flow
Case 6	5	0.48	0.76	1,727	32	0.22	1.08	Orbital

Note. Grain diameter is specified to be 0.44 m in this study.

Abbreviations: T , oscillatory wave period; U_m , free-stream velocity amplitude ($u(t) = U_m \sin(2\pi / T)$); d_0 , orbital excursion length; ψ , mobility number; θ , shields parameter; χ , period parameter.

It is clear that the Wiberg and Harris predictor (1994) parameterizes d_{0m} solely as a function of grain size D_{50} and it is independent of the period parameter. Hence, the entire ripple predictor does not depend on the wave period. On the other hand, both Mogridge et al. (1994) and Nielsen (1981) predictors depend on the period parameter (or the wave period) and grain size. By choosing the onset of ripple regime and sheet flow regime to be at the mobility number $\psi = 10$ and $\psi = 156$, respectively, O'Donoghue and Clubb (2001) further provides the corresponding orbital excursion length, denoted as d_l and d_u , associated with these two demarcations as

$$\frac{d_l}{D_{50}} = \frac{\sqrt{10}}{\pi} \chi^{-0.5}, \quad (23)$$

$$\frac{d_u}{D_{50}} = \frac{\sqrt{156}}{\pi} \chi^{-0.5}. \quad (24)$$

For a given χ , by increasing the orbital excursion length d_0 (increase orbital velocity amplitude for a fixed wave period) beyond d_l , the ripple length increases until reaching the maximum λ_m at corresponding orbital excursion length d_{0m} and this signifies the ripple growing regime. By further increasing d_0 beyond the d_{0m} , ripple length and steepness decrease (the ripple decaying regime) until the sheet flow condition prevails at d_u . By comparing the extensive lab- and field-scale experimental data (including different D_{50} and T) with the different ripple predictors, O'Donoghue et al. (2006) demonstrates that both Mogridge et al. (1994) and Nielsen (1981) predictors lead to good agreement with measured data in the growing regime. However, the Nielsen (1981) predictor underestimates the ripple dimensions in the decaying regime of high mobility number. Hence, O'Donoghue et al. (2006) provides a revised version of the Nielsen (1981) predictor as,

$$\frac{\lambda}{a} = 1.97 - 0.44\psi^{0.21} \quad (25)$$

$$\frac{\eta}{a} = 0.275 - 0.022\psi^{0.42} \quad (26)$$

The ripple regime can be determined by using the mobility number (Nielsen, 1992; O'Donoghue et al., 2006). By choosing the mobility number $\psi = 10$ for the onset of the ripple regime, the transition from the orbital regime to the suborbital and anorbital (decaying regime) occurs at $\psi = 80$, while the transition to sheet flows to occur at $\psi = 156$ (see Table 1). Also, the ripple regime (for a given T and D_{50}) can be obtained by comparing the d_0 to d_m , which is obtained from either Equations 21 or 22, such that for $d_l < d_0 < d_m$, the orbital ripple regime is obtained, and the decaying regime is signified by $d_m < d_0 < d_u$.

Table 2

Simulated Flow Conditions and Predicted λ and η / λ

Case ID	Description	λ_{WH} (m)	$(\eta / \lambda)_{WH}$	λ_M (m)	$(\eta / \lambda)_M$	λ_N (m)	$(\eta / \lambda)_N$	λ_O (m)	$(\eta / \lambda)_O$	λ_f (m)	$(\eta / \lambda)_f$
Case1	$\lambda_i = \lambda_f, \eta_i > \eta_f$	0.47	0.17	0.46	0.18	0.42	0.16	0.40	0.17	0.46	0.17
Case2a	$\lambda_i > \lambda_f, \eta_i > \eta_f$	0.47	0.17	0.36	0.13	0.23	0.07	0.32	0.14	0.345	0.13
Case2b	$\lambda_i > \lambda_f, \eta_i > \eta_f$	0.47	0.17	0.36	0.13	0.23	0.07	0.32	0.14	0.345	0.13
Case3	$\lambda_i > \lambda_f, \eta_i > \eta_f$	0.28	0.17	0.25	0.17	0.24	0.15	0.24	0.17	0.23	0.17
Case4	$\lambda_i < \lambda_f, \eta_i < \eta_f$	0.47	0.17	0.36	0.13	0.23	0.07	0.32	0.14	0.345	0.13
Case5	RTS	SF	SF	SF	SF	SF	SF	SF	SF	SF	SF
Case6	FTR	0.47	0.17	0.46	0.18	0.42	0.16	0.40	0.17	0.46	0.17

Notes. λ_{WH} and $(\eta / \lambda)_{WH}$: Ripple length and steepness predicted by Wiberg and Harris (1994) predictor, respectively. Similarly, the subscripts *N*, *M*, *O*, and *f* represent those calculated by the predictors of Nielsen (1981), Mogridge et al. (1994), O'Donoghue et al. (2006), and the final equilibrium ripple profile of the present numerical model.

Abbreviations: RTS, ripple to sheet flow; FTR, flatbed to ripple; SF: sheet flow condition.

3. Model Results

We present seven numerical experiments to verify the model's capability to predict the expected ripple evolution features. Model results are further analyzed in detail in Section 4 to gain insight into the mechanism driving these compelling bathymetric evolutions. To show if the model predicts the dependency of ripple geometry on the wave period, we designed scenarios Case 1 and Case 2a, in which the $d_0 / D_{50} = 1,727$ ($d_0 = 0.76$ m) is kept the same by using two different combinations of U_m and T (see Table 1). As mentioned before, Case 1 is designed to be similar to Case Mr5b50 from van der Werf et al. (2007) experiment in which $U_m = 0.48$ m/s and $T = 5$ s. The resulting mobility number is $\psi = 32$. The measured equilibrium ripple length is $\lambda_e = 0.46$ m and the steepness is $(\eta / \lambda)_e = 0.17$ (no measured ripple bathymetric profile is reported for this case). The modeled time-series of ripple bed (defined as the contour of volumetric concentration $\phi = 0.57$) evolution and a snapshot of the sediment concentration and velocity fields at the end of the simulation for Case 1 are shown in Figure 2. The initial ripple bed is specified to have a very large steepness of $(\eta / \lambda)_i = 0.26$. After the simulation of about five wave periods (25 s), the decaying ripple height reaches the quasi-steady state with $(\eta / \lambda)_f = 0.17$, which is the same as the steepness of 0.17 reported by van der Werf et al. (2007) and it is also similar to those from the different ripple predictors (see Table 2). In this case, $d_0 / D_{50} = 1,727$, which is close to the condition of maximum equilibrium ripple length and height for the given T and D_{50} before reaching the transition to the suborbital ripple regime. The agreement between measured data, the present modeled data, and those predicted by Wiberg and Harris (1994), Mogridge et al. (1994), and O'Donoghue et al. (2006) are all very good. The Nielsen (1981) predictor slightly under-predicts the ripple's steepness but the agreement is still good.

In Case 2a, the same three-ripples profile used in Case 1 with higher-than-expected steepness is used for the initial bed profile. However, Case 2a is forced with a higher velocity amplitude $U_m = 0.8$ (m/s), and shorter flow period $T = 3$ s which results in the same $d_0 = 0.76$ m (or $d_0 / D_{50} = 1,727$) as in Case 1. The larger velocity amplitude causes a near factor three increase of the Shields parameter exceeding $\theta = 0.6$ (or mobility number $\psi = 90$) while the shorter period also increases the period parameter by nearly a factor of three. We will later discuss more thoroughly that the ripples in Case 2a are in the decaying regime and the ripple length and height are both expected to become smaller. As shown in Figure 3a, these three ripples evolve from three large ripples (at $t = 0$) to four smaller ripples through sliding, merging, and protruding of new ripples in-between the initial larger ripples. After 80 wave periods ($t = 240$ s), four smaller ripples with a length of $\lambda_f = 0.345$ m and steepness of $(\eta / \lambda)_f = 0.13$ are obtained. We continue the simulation for 20 more periods ($t = 240$ –300 s) to ensure that the simulation has reached the quasi-equilibrium state.

It is important to confirm that for the given grain size and wave condition, model results are not sensitive to the initial ripple profile. In Case 2b, the simulation starts with the final flow field and ripple profile of

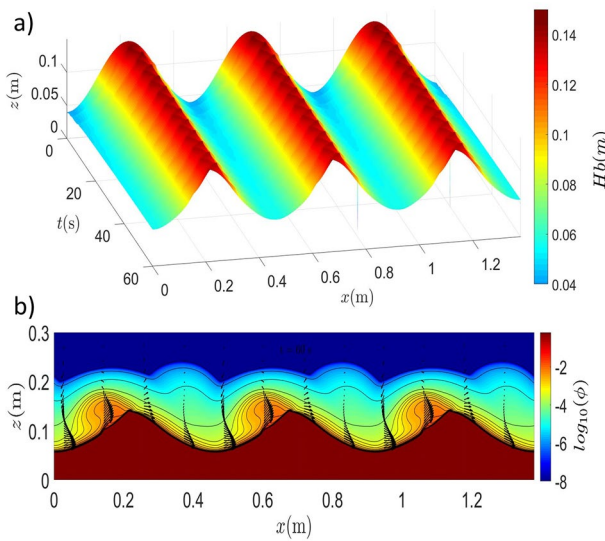


Figure 2. (a) Time series of ripple bed evolution (for Case 1) with the color shows the bed level height defined as the iso-contour of $\phi = 0.57$. (b) Final ripple-bed profile at $t = 60$ s with the color represents sediment volumetric concentration in log scale and the vectors signify the velocity field.

Case 1, but the newly applied wave forcing is identical to that of Case 2a. Therefore, Case 2b is the continuation of the simulation of Case 1 but with a sudden change of the wave orbital motion. Model results for Case 2b are provided in Figure 3b. The final ripple bed profile of Case 2b is nearly identical to that obtained in Case 2a (compare bottom panels in Figures 3a and 3b), especially in terms of the final ripple lengths and steepness (see Table 2). However, it only takes about 60 wave periods (180 s) to reach the equilibrium state of the ripple profile in Case 2b, which is about 20 wave periods (60 s) shorter than the time required for Case 2a. Again, we continued the simulation of Case 2b for another 20 wave periods to ensure that the equilibrium state has been reached. Numerical experiments presented here confirm that the equilibrium ripple geometry is independent of the initial ripple profile, but the time needed to reach the equilibrium state is sensitive to the initial ripple profile (Doucette & O'Donoghue, 2006).

As shown in Table 2, the modeled ripple length in Case 2 $\lambda_f = 0.345$ m is slightly shorter than that calculated by the Mogridge et al. (1994) predictor $\lambda_M = 0.36$ m, while the modeled ripple steepness is the same as that predicted by Mogridge et al. (1994) (i.e., $(\eta / \lambda)_f = (\eta / \lambda)_M = 0.13$). Specifically, for the given χ in Case 2, Equation 22 gives the $d_{0m} = 0.58$ m and consequently $\lambda_m = 0.36$ m (or use Equation 17). As the orbital excursion length in Case 2, $d_0 = 0.76$ m, is notably larger than d_{0m} , the ripple is in the decaying regime and λ_f should be smaller than λ_m . In other

words, ripples in Case 2 can be classified as suborbital ripples. Since the Mogridge et al. (1994) predictor cannot predict the reduction of ripple length in the decaying regime, the slightly shorter ripple length predicted by the present model when compared to that of Mogridge et al. (1994) is expected. The result is also qualitatively consistent with Nielsen's (1981) formulation as the mobility number in Case 2 is high $\psi = 90$. However, Nielsen (1981) predicts a much more rapid decay of ripple dimensions ($\lambda_N = 0.23$ m ($\eta / \lambda)_N = 0.07$) in high mobility number ranges beyond the orbital ripple, an issue that has already been raised by O'Donoghue and Clubb (2001) and O'Donoghue et al. (2006). Since the Wiberg and Harris (1994) predictor does not depend on the wave period, according to Equation 20, it predicts that the ripples in

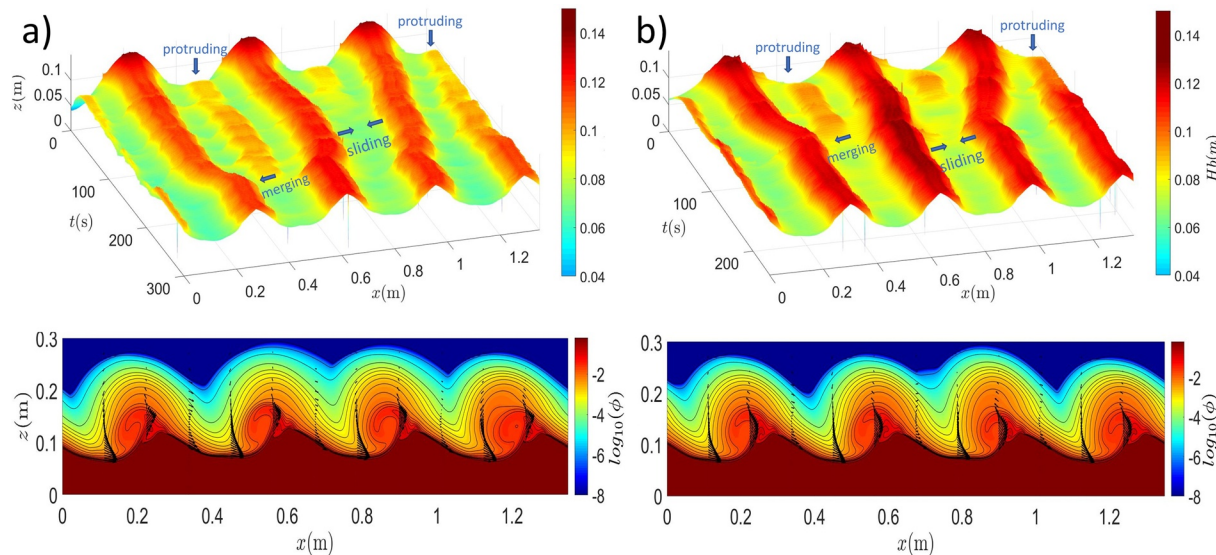


Figure 3. (a) The top panel shows the time series of ripple bed evolution for Case 2a with the color represents the bed level defined as the contour of $\phi = 0.57$ and the bottom panel shows the final ripple-bed profile at $t = 300$ s with color represents volumetric concentration in log-scale and the vectors signify the velocity field. (b) The corresponding ripple bed evolution (top panel) and final bed profile ($t = 240$ s, bottom panel) for Case 2b.

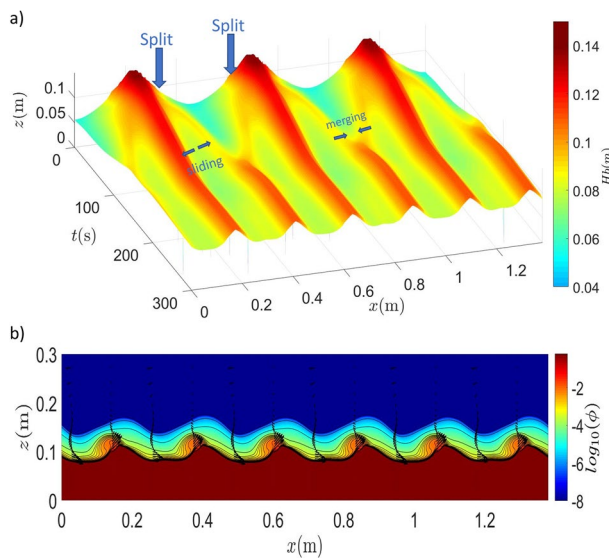


Figure 4. (a) Time series of ripple bed evolution for Case 3 with the color represents the bed level height defined as the contour of $\phi = 0.57$. (b) Final ripple-bed profile at $t = 240$ s with the color shows sediment volumetric concentration in log-scale and the vectors represent the velocity field.

steepness is in the orbital ripple regime of $(\eta / \lambda)_M = (\eta / \lambda)_O = 0.17$ and $(\eta / \lambda)_N = 0.15$. Using the same model domain length of $L_x = 1.38$ m, we expected to obtain about 5–6 ripples at the equilibrium stage. It is worth pointing out that the mobility numbers between Case 1 and Case 3 are identical and hence Case 3 allows us to solely evaluate the model's capability to capture the effect of changing the wave orbital excursion length. Because the Swart (1974) formula used here for calculating the friction factor (Equation 15) also depends on the wave period, a shorter wave period in Case 3 gives a slightly larger Shields parameter (0.26) than that of Case 1 (0.22).

Figure 4 shows the model results for Case 3. Modeled ripple length $\lambda_f = 0.23$ m is in good agreement with those calculated by Nielsen (1981) and O'Donoghue et al. (2006) predictors. However, the modeled ripple steepness $(\eta / \lambda)_f = 0.17$ is larger than that predicted by Nielsen (1981), $(\eta / \lambda)_N = 0.15$, but agrees with other predictors expected for orbital ripples. It is clear from Figure 4 that due to the reduction in the orbital excursion length, the smaller ripples are split from either side of each initial longer ripple. The split ripples then slide away and migrate toward the troughs of the initial ripples where they merged into each other to form a new equilibrium ripple. After 80 wave periods ($t = 240$ s), the formation of six shorter ripples become evident. After full merging of the smaller ripples in the trough locations at $t = 120$ s and until about $t = 180$ s (60th wave period), these smaller ripples slowly increase their height while the original large ripples reduce their height. After the 60th wave period ($t = 180$ s), the ripples seem to reach the equilibrium state. More insight into the mechanism of the smaller ripples formation from larger ripples due to the reduction of orbital excursion length will be discussed in Section 4.

During storm conditions, ripples are observed to grow, both in length and height, by merging smaller ripples (Traykovski et al., 1999). To further test SedFoam's capability in predicting growing ripples, in Case 4 we initialize the bed profile using the final ripple bed obtained in Case 3. Then, the model is forced by the wave forcing used in Case 2. Compared to Case 3, we increase the orbital velocity amplitude to $U_m = 0.8$ m/s while maintaining the wave period to be $T = 3$ s and hence the orbital excursion length is also increased (see Table 1). The ripples length is expected to grow while the ripple steepness reduces due to the transition from orbital to suborbital ripples. Among the initial six small ripples (Figure 5a), four of them (those four located between $x = 0.55$ – 1.38 m) form two pairs and start to merge with each other, becoming two larger ripples within the first 20 wave periods (60 s). Meanwhile, the other two isolated ripples initially located

Case 2 remain in the orbital ripple regime with much longer and steeper ripples ($\lambda_{WH} = 0.47$ m, $(\eta / \lambda)_{WH} = 0.17$) than the present model results. Finally, model results agree well with the ripple predictor of O'Donoghue et al. (2006), which indicates a shorter ripple of $\lambda_o = 0.32$ m with a steepness of $(\eta / \lambda)_o = 0.14$. Overall, the two-phase model SedFoam confirms that ripple geometry depends on the wave period (Mogridge et al., 1994). The model can also reproduce the ripple decaying regime consistent with the ripple geometry predicted by O'Donoghue et al. (2006). The small discrepancy in the predicted ripple length (about 7% error) may simply be due to the limitation of the periodic boundary condition applied at the two lateral boundaries.

To simulate the ripple evolution under the waning wave orbital motion, in Case 3 the orbital excursion length is decreased to $d_0 = 0.46$ m by specifying the velocity amplitude to $U_m = 0.48$ (m/s) and wave period $T = 3$ s. The orbital excursion length in Case 3 is nearly 40% smaller than that in Case 1 (due to reducing T) and Case 2 (due to reducing U_m). The resulting mobility number is $\psi = 32$ (Shields parameter $\theta = 0.26$, see Table 1). This flow condition is applied to the final ripple profile obtained in Case 1. In this case, $d_0 / D_{50} = 1,040$, and based on the Wiberg and Harris (1994) predictor, the ripple is in the orbital ripple regime with $\lambda_{WH} = 0.28$ m and $(\eta / \lambda)_{WH} = 0.17$. The Mogridge et al. (1994), Nielsen (1981), and O'Donoghue et al. (2006) predictors suggest slightly shorter ripple length of $\lambda_M = 0.25$ m and $\lambda_N = \lambda_O = 0.24$ m, respectively, while the ripple

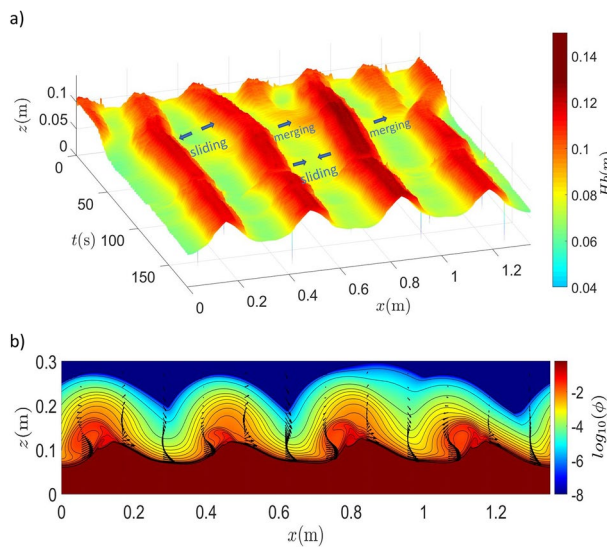


Figure 5. (a) Time series of ripple bed evolution for Case 4 with the color represents the bed level height defined as the contour of $\phi = 0.57$. (b) Final ripple-bed profile at $t = 180$ s with the color shows sediment volumetric concentration in log-scale and the vectors represent the velocity field.

between $x = 0.05\text{--}0.5$ m simply grow larger locally and adjust their positions by sliding away from each other. At about 25 wave periods into the simulation ($t = 75$ s), four large ripples have more or less been established while mild sliding movements continue to occur to adjust their relative distance. At the end of the 30 wave periods ($t = 90$ s), we obtain four equal-sized ripples similar to those seen at the end of the Case 2 simulation (see Figure 3). This result again confirms that the final equilibrium ripple profile is independent of the initial bed state, although the time to establish the equilibrium ripple bed depends on the initial bed.

In Case 5, we apply a more dramatic increase of wave orbital velocity to evaluate the model's capability to simulate the transition from ripple bed to sheet flow. The simulation is initialized with the final ripple bed profile obtained in Case 1. We apply an oscillatory flow following the same wave period of $T = 5$ s as Case 1, however, the orbital velocity amplitude is increased to $U_m = 1.5$ m/s ($d_0 = 3.14$ m, which is much beyond the $d_u = 1.47$ m, see Equation 24) and the Shields parameter is $\theta = 1.53$ (see Table 1). Due to the very energetic wave motion, ripple steepness decreases drastically during the first two wave cycles from the initial value of $\eta / \lambda = 0.17$ to about 0.065 (see Figure 6a). Afterward, the ripple steepness decays more slowly. After only 12 wave periods ($t = 60$ s), the ripple steepness reduces to $\eta / \lambda = 0.0075$ and the bed is essentially flat.

Using the final bed profile obtained in Case 5 as the initial bed profile, we test the model's capability in Case 6 to simulate the formation of a ripple bed from a nearly flat bed ($\eta / \lambda = 0.0075$). The same oscillatory flow forcing used in Case 1 is applied in Case 6 and three orbital ripples are expected in the final bed profile. At the beginning of this simulation (Figure 6b), several smaller “grain rolling ripples” start to form during the first few periods, and no vortices are observed. After the steepness of these smaller ripples becomes sufficiently large ($t = 60$ s), vortices start to form and the small ripples merge into each other to form larger ripples. Finally, the equilibrium state with λ_f and $(\eta / \lambda)_f$ nearly identical to those of Case 1 is reached at $t = 300$ s (60 wave periods). In general, the time needed for a bed to reach equilibrium due to a step-change in the

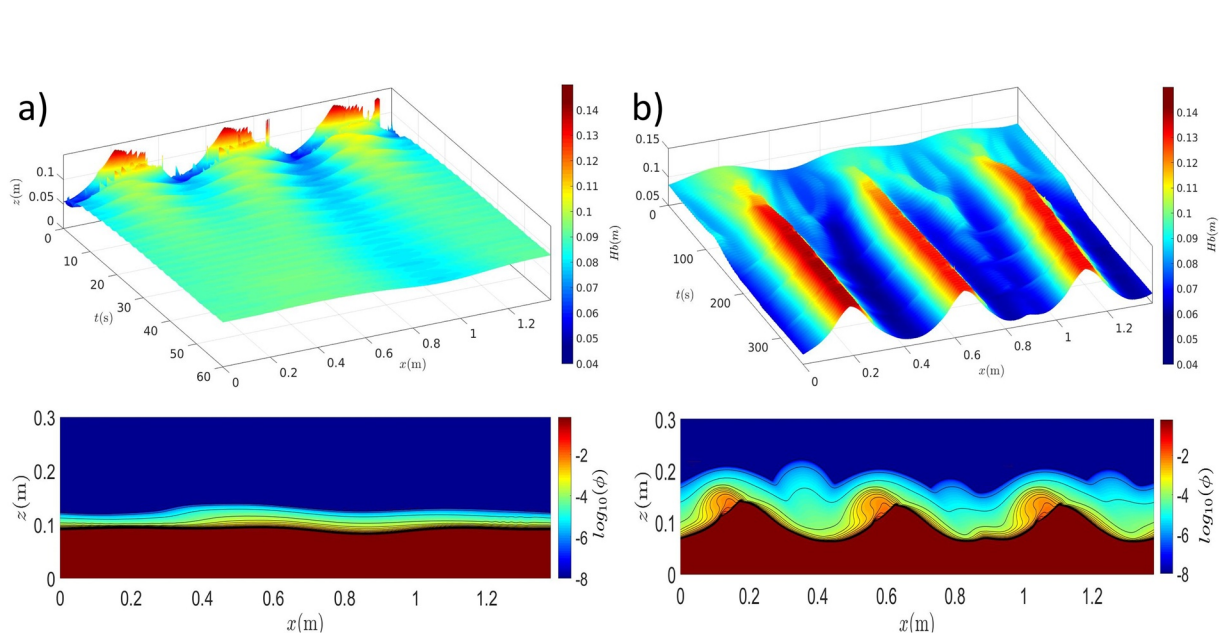


Figure 6. (a) The top panel shows the time series of ripple bed evolution into sheet flow for Case 5 with the color shows the bed level defined as the contour of $\phi = 0.57$ and the low panel shows the final bed profile at $t = 60$ s with color represents volumetric concentration in log-scale. (b) The corresponding ripple bed evolution (top panel) and final bed profile ($t = 300$ s, lower panel) for Case 6.

flow forcing is underestimated in the present 2DV model when compared to the laboratory experiment or field observation. For example, Testik et al. (2005) and Voropayev et al. (1999) introduce a ripple evolution time scale as,

$$\tau = \frac{C}{\omega \sqrt{\psi}} \quad (27)$$

which includes both the effect of the wave period and the sediment size, and $C = 2,500$ is an empirical constant. Starting from a flat bed, they showed that after $t_e = 3\tau$ ripples reach 95% of their equilibrium dimensions. Using Equation 27 for Case 6 results in $\tau = 352$ s and $t_e \approx 1000$ s which is more than three times longer than the modeled evolution time ($t = 300$ s). The modeled evolution timescales are consistent with those obtained by Penko et al. (2011) who used the mixture approach for simulating 2D ripple evolution. Later, Penko et al. (2013) carried out 3D simulations and obtain slower evolution time. They argue that the initial stage of the ripple developments are 3D phenomena with defects and irregularities during the evolution. Hence, the abovementioned evolution time discrepancy may be due to these 3D effects.

In summary, the model results for ripple geometry in the equilibrium state are in good agreement with ripple predictors that include the flow period in their formulations (O'Donoghue et al., 2006). Specifically, for a given sediment size, the transition from the ripple growing regime to the decaying regime depends on the flow period, such that under the same orbital excursion length, a flow with a shorter period and higher velocity amplitude generates smaller ripples compare to a flow with a longer period and lower velocity amplitude. In addition to the growing (orbital) and decaying (suborbital) regimes, the model is capable of simulating the formation of smaller ripples from larger ripples, and the regrowth to larger ripples from smaller ripples, through splitting, sliding, and merging processes. In the two limiting scenarios, the model can simulate the ripple washout to sheet flow condition, and the ripple bed formation from a nearly flat bed. However, due to the complex coupling between the hydrodynamics and the sediment transport, until now there is not a clear physical explanation of the period effect on the equilibrium ripple geometry and the transient evolution, or the relative importance between the near-bed load and the suspended load in different regimes (Traykovski et al., 1999; Wiberg & Harris, 1994). The following section is dedicated to investigating these issues.

4. Discussion

4.1. Orbital and Suborbital Ripples in the Equilibrium State

In order to gain physical insights into the transition between orbital and suborbital ripple regimes, the flow and sediment fields in Case 1 and Case 2b are examined. Figure 7 is organized to show the sediment concentration and velocity (left panels) fields, normalized vorticity field [$\Omega / \omega = 1 / \omega (\partial w^f / \partial x - \partial u^f / \partial z)$] (middle panels) and nondimensional sediment flux [$\Psi = q / \sqrt{(s-1)gD_{50}^3}$] (right panels, in which $q = \phi u^s$) for Case 1 and Case 2b, respectively. Due to the symmetric flow between the onshore (positive velocities pointing to the right) and offshore (negative velocities pointing to the left) phases, two representative time instants during the onshore phase are chosen for the purpose of comparison. During the off-onshore flow reversal (Figures 7a1 and 7a2), both cases show two vortices structures above the offshore (left side) ripple flanks: a larger primary vortex (with positive vorticity), which is generated during the previous offshore flow cycle, and a smaller secondary vortex (with negative vorticity) underneath the primary vortex attached to the ripple's surface. However, some notable differences between these two cases can be observed. The cloud of the suspended sediment associated with the primary vortex in the suborbital ripple Case 2b (see left panel of Figure 7a2) is significantly larger than the one in the orbital ripple Case 1 (left panel in Figure 7a1). The Shields parameter in Case 2b is about three times larger than that in Case 1, and the larger suspended load in Case 2b is consistent with the Wiberg and Harris (1994), which indicated that in the suborbital ripple regime, the boundary layer thickness is larger than the ripple height (i.e., $\delta_w > \eta$). Furthermore, the primary and secondary vortex intensities are nearly a factor three larger in Case 2b compare to Case1 (compare the middle panels in Figures 7a1 and 7a2). Therefore, both the sediment flux near the ripple's surface on the offshore flank (onshore-directed, red color) and the suspended flux associated with the primary vortex

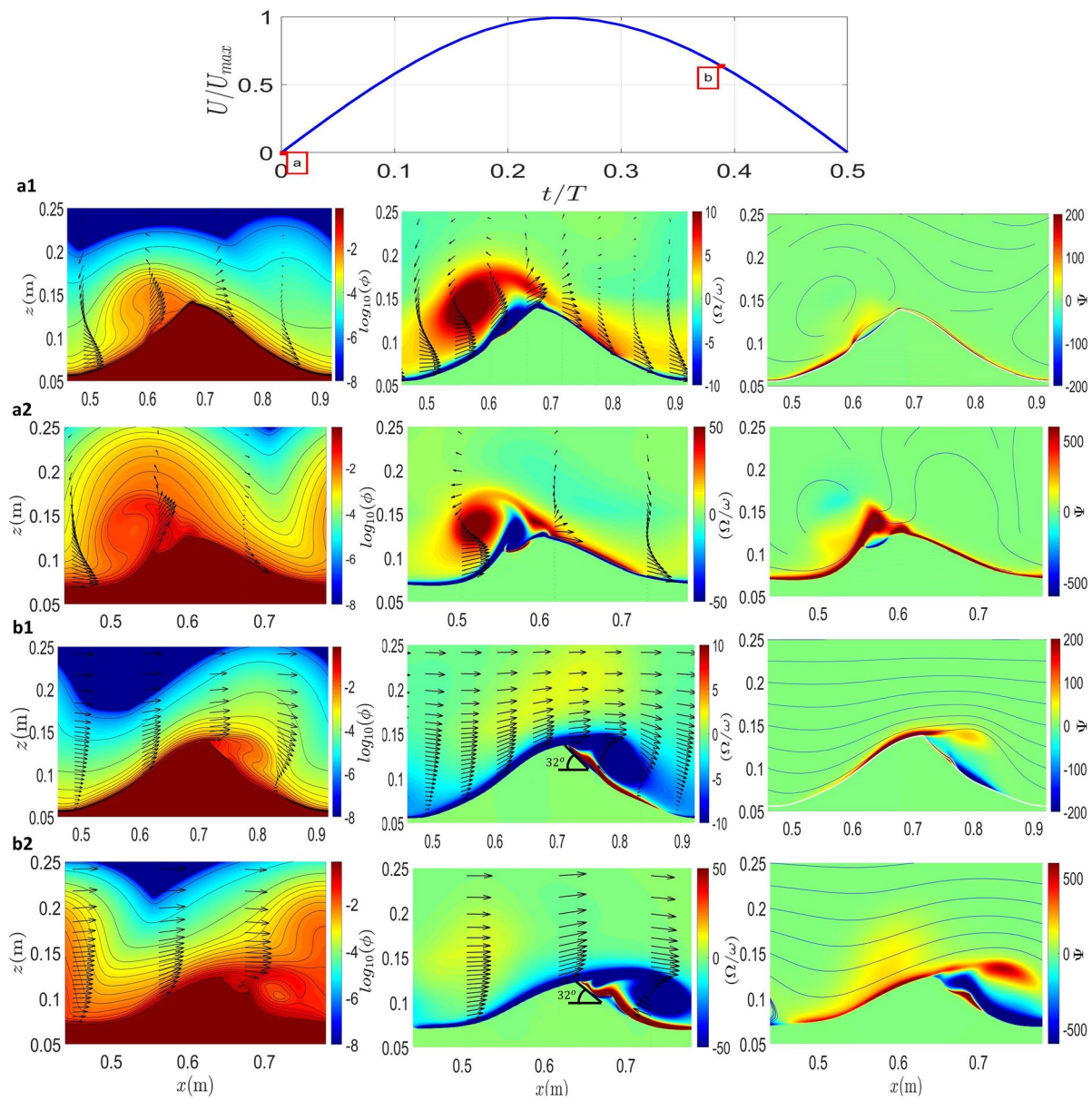


Figure 7. Snapshots of color contours for modeled sediment concentration field (left panels), normalized vorticity field (middle panels), and sediment horizontal flux (right panels) for two instants (a) and (b) during the positive velocity period for Case 1 (orbital ripple, indicated by a1 and b1) and Case 2b (suborbital ripple, indicated by a2 and b2). In each panel, the velocity field is down-sampled and represented by the vectors. The blue lines in the right panels represent the flow streamlines. The top panel shows the time series of free-stream velocity and the corresponding two instants (a) and (b) are indicated.

(offshore-directed) are significantly larger in Case 2b compared to those in Case 1 (right panels in Figures 7a1 and 7a2). During the onshore deceleration phase (middle panels in Figures 7b1 and 7b2), the secondary vortex (positive vorticity) on the onshore flank becomes more obvious. Meanwhile, sediment avalanching occurs locally as the flank slope exceeds the angle of repose (see the positive sediment flux on the onshore ripple flanks underneath the negative flux triggered by the returning boundary layer flow). Again, these features are more pronounced in Case 2b. Importantly, in Case 2b, the primary vortices are large enough to reach the ripple trough and influence the flow and sediment transport of the adjacent ripple. Although the patterns of the vortex generation-ejection process and the associated sediment fluxes are similar in equilibrium orbital and suborbital ripples, the relative size and intensity of the vortices and the resulting sediment fluxes are significantly larger in the suborbital ripple regime (Case 2b).

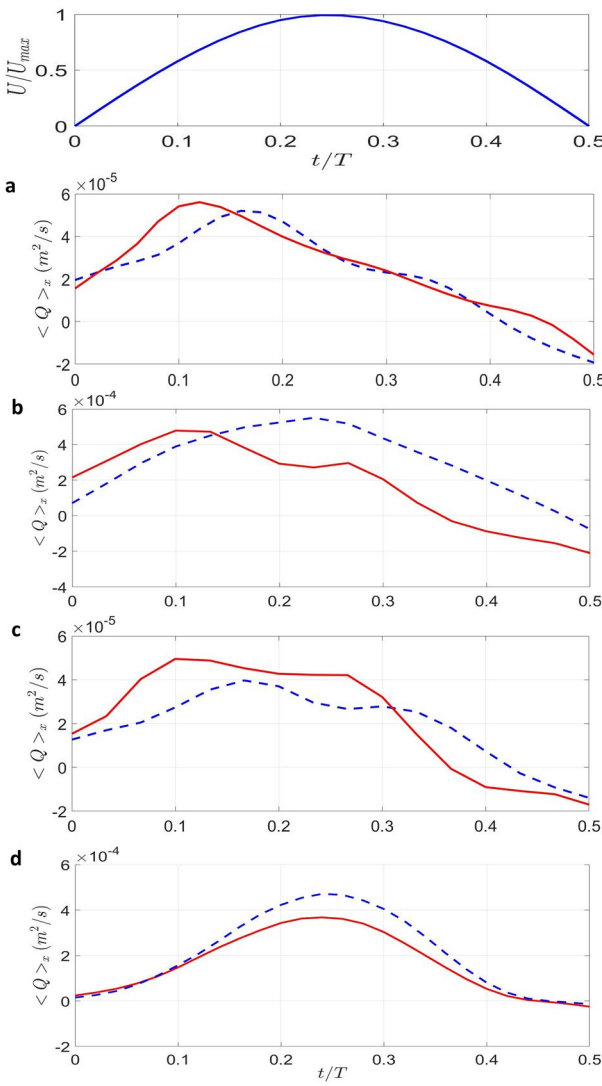


Figure 8. Time series of near-bed load transport rate (red-solid line) and suspended load transport rate (blue-dashed line) for Case 1 (a), Case 2b (b), Case 3 (c), and Case 5 (d). The top panel shows the free stream velocity time series for half a period normalized by the orbital velocity amplitude.

(see Figure 8b) and the ratio is $R = 1.73$. It should be also noted that the overall magnitude of sediment transport rates, regardless of suspended load or near-bed load, are nearly an order of magnitude larger in Case 2b. Our model results are consistent with the hypothesis proposed by Traykovski et al. (1999) that under the same wave orbital excursion length, the near-bed load transport is dominant for the flow with the longer period and lower velocity (smaller Shields parameter or mobility number) while the suspended load is conducive to a shorter-period wave with higher velocities. Also, the dominance of suspended load in Case 2b is consistent with several studies (e.g., Ribberink et al., 2008; van der Werf et al., 2006; Wiberg & Harris, 1994) which show that the suspended load is dominant in suborbital and anorbital regimes.

4.2. Quantifying Bed State Using the Suspended Load to Near-Bed Load Ratio

Motivated by the analysis presented in Section 4.1 for an orbital ripple case (Case 1) and a suborbital case (Case 2), we investigate if the suspended load to near-bed load ratio, R , can be used to quantify the bed state

To better quantify the more significant contribution of suspended load in the suborbital ripple regime, we calculate the time series of the horizontally-averaged (or ripple-averaged, $\langle \cdot \rangle_x$) near-bed load transport rate Q_b and suspended load transport rate Q_s (see Figure 8). Here, the near-bed load transport rate accounts for the transport from the bottom of the domain to the vertical location z_{so} where sediment concentration $\phi = 0.08$. This volumetric concentration criterion has been proposed by earlier sediment transport studies (Dohmen-Janssen & Hanes, 2002; Lanckriet & Puleo, 2015) as it represents the averaged distance among spheres to be one particle diameter. The bedload transport rate is calculated as,

$$Q_b = \int_{z=0}^{z=z_{so}} q(z) dz \quad (28)$$

The suspended load transport rate is then defined as transport above $z = z_{so}$ to the top of the model domain:

$$Q_s = \int_{z=z_{so}}^{z=L_z} q(z) dz \quad (29)$$

Since Case 1 and Case 2b are driven by sinusoidal wave motion, both the near-bed load transport and the suspended load transport are symmetric in onshore and offshore phases and the net transport rate is zero in the equilibrium state. In Case 1 (orbital ripple), the suspended load sediment flux Q_s is generally smaller than or similar to the near-bed load flux Q_b (see Figure 8a). On the other hand, the suspended sediment flux Q_s is mostly (about three quarter of a period) larger than the near-bed load flux Q_b in Case 2b (suborbital ripple, Figure 8b) except for the interval during flow reversal. To quantify the relative importance between the suspended load and near-bed load, we calculate the half-period-averaged suspended load transport rate $\langle Q_s \rangle_{T/2}$ and the near-bed load transport rate $\langle Q_b \rangle_{T/2}$. In the orbital ripple Case 1, the half-period-averaged suspended load transport rate is $\langle Q_s \rangle_{T/2} = 1.85 \times 10^{-5} (m^2/s)$ and the corresponding near-bed load transport rate is $\langle Q_b \rangle_{T/2} = 2.5 \times 10^{-5} (m^2/s)$. Hence, the suspended load transport rate is smaller and the suspended load to near-bed load ratio is $R = \langle Q_s \rangle_{T/2} / \langle Q_b \rangle_{T/2} = 0.74$. On the other hand, in the suborbital ripple Case 2b, the half-period-averaged suspended load transport rate is $\langle Q_s \rangle_{T/2} = 3.05 \times 10^{-4} (m^2/s)$, which is notably larger than the near-bed load transport rate of $\langle Q_b \rangle_{T/2} = 1.76 \times 10^{-4} (m^2/s)$

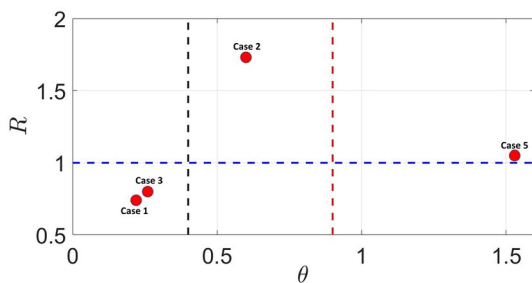


Figure 9. Suspended load to near-bed load ratio (R) as a function of Shields parameter (θ) for different cases investigated in this study.

is mostly larger, although only slightly, than the near-bed load transport rate except for near flow reversal (Figure 8d).

In Figure 9, the half-period-averaged suspended load to near-bed load ratio, R , is plotted against the Shield parameter, θ , for all cases. In this plot, $\theta = 0.4$ and 0.9 are calculated as the demarcations between the ripple growing and the decaying regime, and the ripple transition to sheet flow by using $\psi = 75$ and $\psi = 154$, respectively. For the given sediment size $D_{50} = 0.44$ mm, it is shown in Section 4.1 that for Case 1 and Case 2b with the same d_0 / D_{50} , the suspended load is dominant in Case 2b with a smaller period and a larger velocity. As indicated in Figure 9, Case 2b has a higher Shields number at $\theta = 0.6$ and large $R = 1.73$, while Case 1 is of low Shields parameter $\theta = 0.22$ and small $R = 0.74$. This can also be interpreted as an increase of the bottom shear stress (or friction velocity) and a decrease in the Rouse number w_s / U_m , as the sediment settling velocity (w_s) is the same for both cases but a higher free stream velocity amplitude U_m in Case 2b. In Case 3, the Shields parameter is slightly larger than that of Case 1, and the suspended load to near-bed load ratio $R = 0.8$ is also slightly larger. Because Case 1 and Case 3 have the same mobility number, the Shields parameter appears to be a better nondimensional parameter than the mobility number to characterize the bed state due to the consideration of wave friction factor (see Equation 15). In the sheet flow condition of Case 5, $R = 1.08$ is slightly larger than unity. O'Donoghue and Wright (2004) shows that in the sheet flow condition, R depends on the grain size and it can be notably larger (for finer sand) or even smaller (for coarser sand) than unity. In summary, for the present medium to coarse sand condition with $D_{50} = 0.44$ mm, Figure 9 shows strong evidence that sediment transport in the orbital ripple regime is near-bed load dominated with $R < 1$. However, sediment transport in the suborbital ripple regime is suspended load dominated with $R > 1$. It can be expected that in a higher Shields parameter range ($\theta > 0.6$) of an orbital ripple regime, the suspended load to near-bed load ratio, R , should decrease toward unity as sheet flow prevails.

4.3. Adjustment to Equilibrium and the Role of Vortices

The previous subsection establishes the suspended load to near-bed load ratio for four different bathymetric features at the equilibrium condition. However, before the equilibrium state is reached, the relative importance between near-bed load and suspended load varies. In Case 1, the initial ripple height is larger than the equilibrium ripple height, hence significant sediment transport occurs to adjust the bed features. In Case 1, because the fluid and sediment velocities throughout the domain are initialized as zero, near-bed load flux was much larger than the suspended load flux during the first wave period. However, between the second and the end of the third wave period, the suspended load became more significant in contributing to the morphological adjustment. In the subsequent wave periods, the contribution from the suspended load begins to reduce, and after about the eighth wave period, the relative contributions between suspended load and near-bed load reached equilibrium as well as the morphological evolution. A more detailed discussion on these interesting time-dependent features during the adjustment to equilibrium ripples are discussed next.

using different cases simulated in this study. At the equilibrium stage, the half-period time series of suspended load transport rate and near-bed load transport rate for Case 3 (orbital ripple), and Case 5 (sheet flow) are presented in Figures 8c and 8d. Comparing Case 3 and Case 1, the velocity amplitude is kept the same but the wave period is reduced in Case 3. Hence, the mobility number is kept the same, but d_0 / D_{50} is reduced (see Table 1). The wave friction factor (Equation 15) and the resulting Shields parameter are slightly increased due to the decreasing wave period. Figure 8c shows the time series of the suspended load transport rate and near-bed load transport rate of Case 3 for half a wave period. The near-bed load transport rate is almost always larger than the suspended load transport rate, except around the time of the deceleration phase ($t / T = 0.31 - 0.37$) when the vortex generation-ejection process occurs. For the sheet flow condition of Case 5, the suspended load transport rate

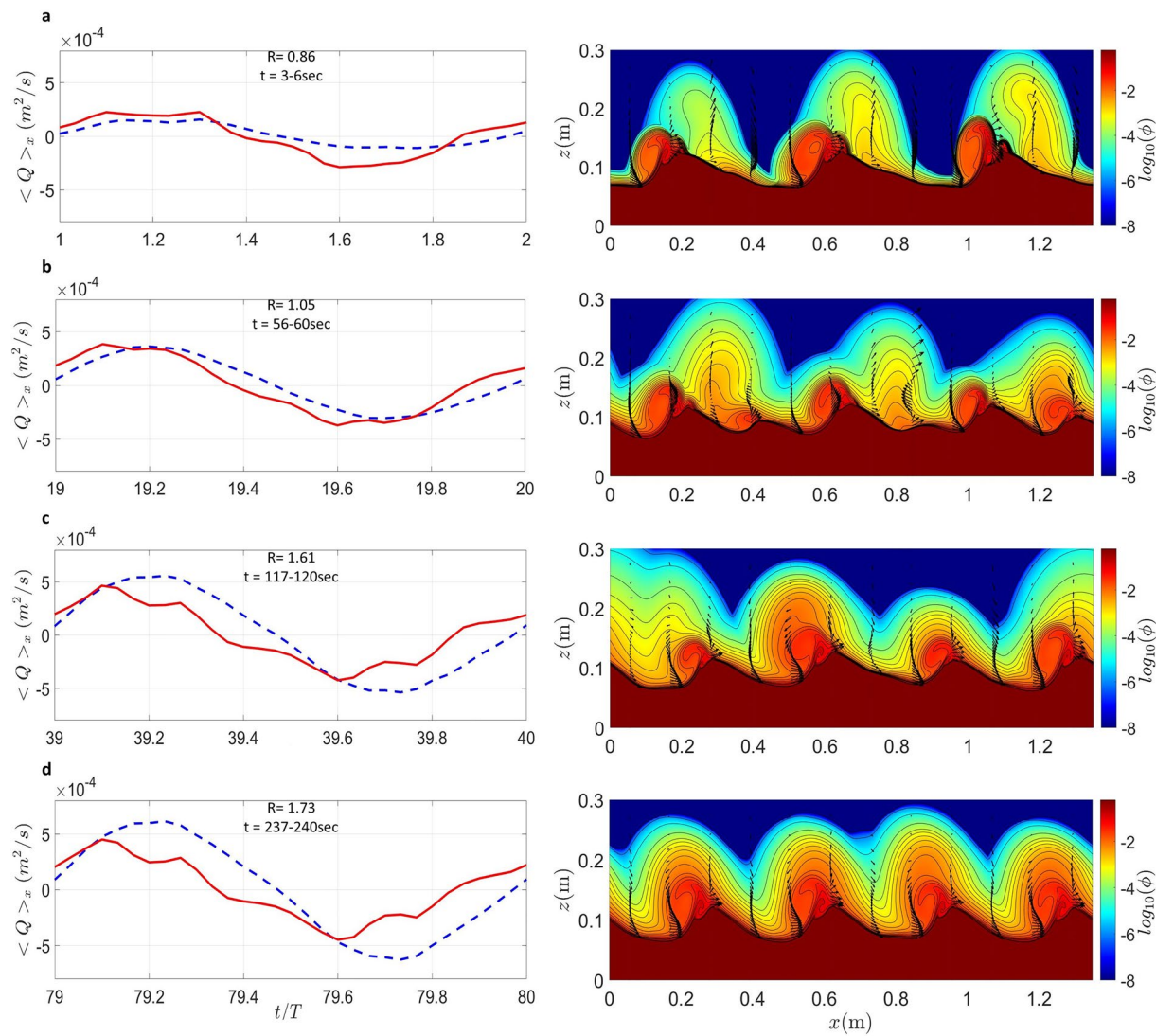


Figure 10. Time series of near-bed load transport (red-solid line) and suspended load (blue-dashed line) for Case 2b during different time intervals (left panels) and the corresponding snapshot at the end of the time-series (right panels) for (a) the second wave period, (b) 20th wave period, (c) 40th wave period, (d) 80th wave period. The suspended load to near-bed load ratio R is also indicated in each of the left panel.

For both Case 2b and Case 3, the simulations are initialized with the more realistic equilibrium ripple geometry of Case 1. Due to the new oscillatory forcing, the initial ripple height and length must evolve into a new equilibrium state. In Case 2b, suborbital ripples are obtained at the equilibrium stage and the near-bed load flux is significantly smaller than the suspended load flux ($R = 1.73$, see Figure 9). Interestingly, during the early stage of the temporal evolution (see Figure 10a at $t = 3\text{-}6\text{ s}$, the second wave periods), the near-bed load is larger than the suspended load. As the simulation continues, the contribution from the near-bed load decreases. At $t = 57\text{-}60\text{ s}$ (20th wave period, Figure 10b) the near-bed load and suspended load are of similar magnitude. During this early stage of the evolution, the initial larger ripples slide away from each other slightly, while the ripple shapes become skewed (right panel in Figure 10a). In between these ripples, the bed is then protruded and smaller ripples start to emerge (see the right panel in Figure 10b). During this process, the ripples slide away from (or toward) each other and a smaller vortex generation-ejection process begins to occur in the trough of the larger ripples. The ripple formed at $x = 1.3\text{ m}$ is the largest one among the newly formed ripples and it grows in time to form a larger ripple (see the right panel in Figure 10c). Between $t = 60$ and 120 s , the smaller ripple that emerged at $x = 0.4\text{ m}$ merge into the onshore flank of the ripple located at the offshore side while the one located at $x = 0.9\text{ m}$ is absorbed by the two adjacent larger

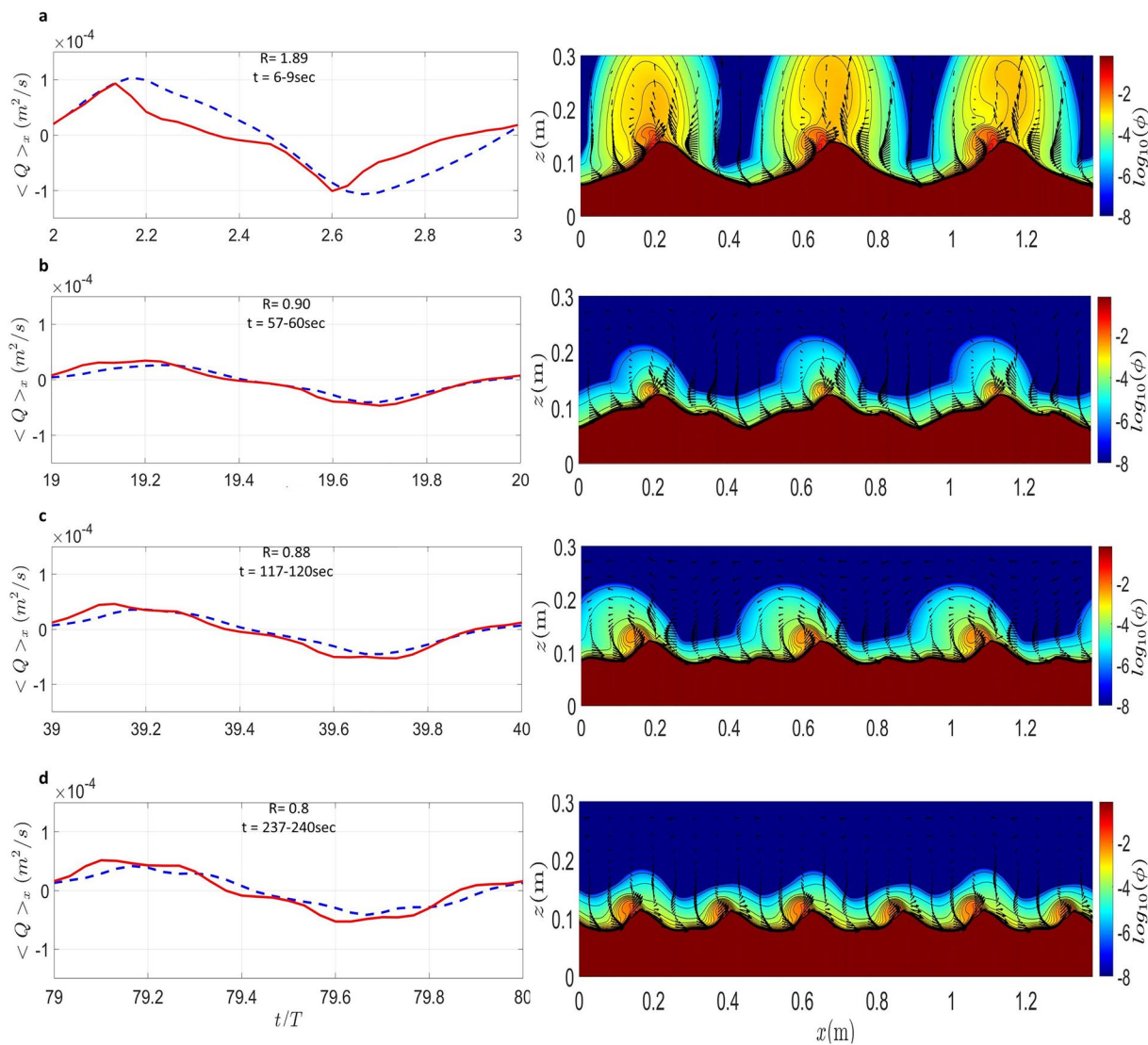


Figure 11. Time series of near-bed load transport (red-solid line) and suspended load (blue-dashed line) for Case 3 during different time intervals (left panels) and the corresponding snapshot at the end of the time-series (right panels) for (a) the third wave period, (b) 20th wave period, (c) 40th wave period, (d) 80th wave period. The suspended load to near-bed load ratio R is also indicated in each of the left panel.

ripples as they slide toward each other. At this stage, the suspended load clearly becomes dominant (see left panel of Figure 10c). Between $t = 120$ and 240 s the four newly formed ripples adjust their height and length to reach the equilibrium (see the right panels in Figures 10c and 10d). During this final stage of evolution, due to generation and ejection of the larger vortices, the suspended load is the dominant mode of transport (see the left panels in Figure 10d), consistent with the final equilibrium stage of suborbital ripple regime discussed in Figure 8b.

In Case 3, during almost the entire evolution process, the near-bed load is greater than the suspended load by a small fraction (see the left panels in Figures 11b–11d) except at the beginning of the simulation when the ripples are much larger than the equilibrium (Figure 11a). The dominance of near-bed load is expected as the ripple bed is in the orbital ripple regime. However, the evolution to smaller ripples in this case is different from the evolution to smaller ripples in Case 2b (suborbital regime). In this case, smaller ripples start to split from the initial ripples' flank (see the right panel in Figure 11b). These smaller ripples move toward each other and then merged into each other at the initial ripples' trough (right panel in Figures 11c–11d).

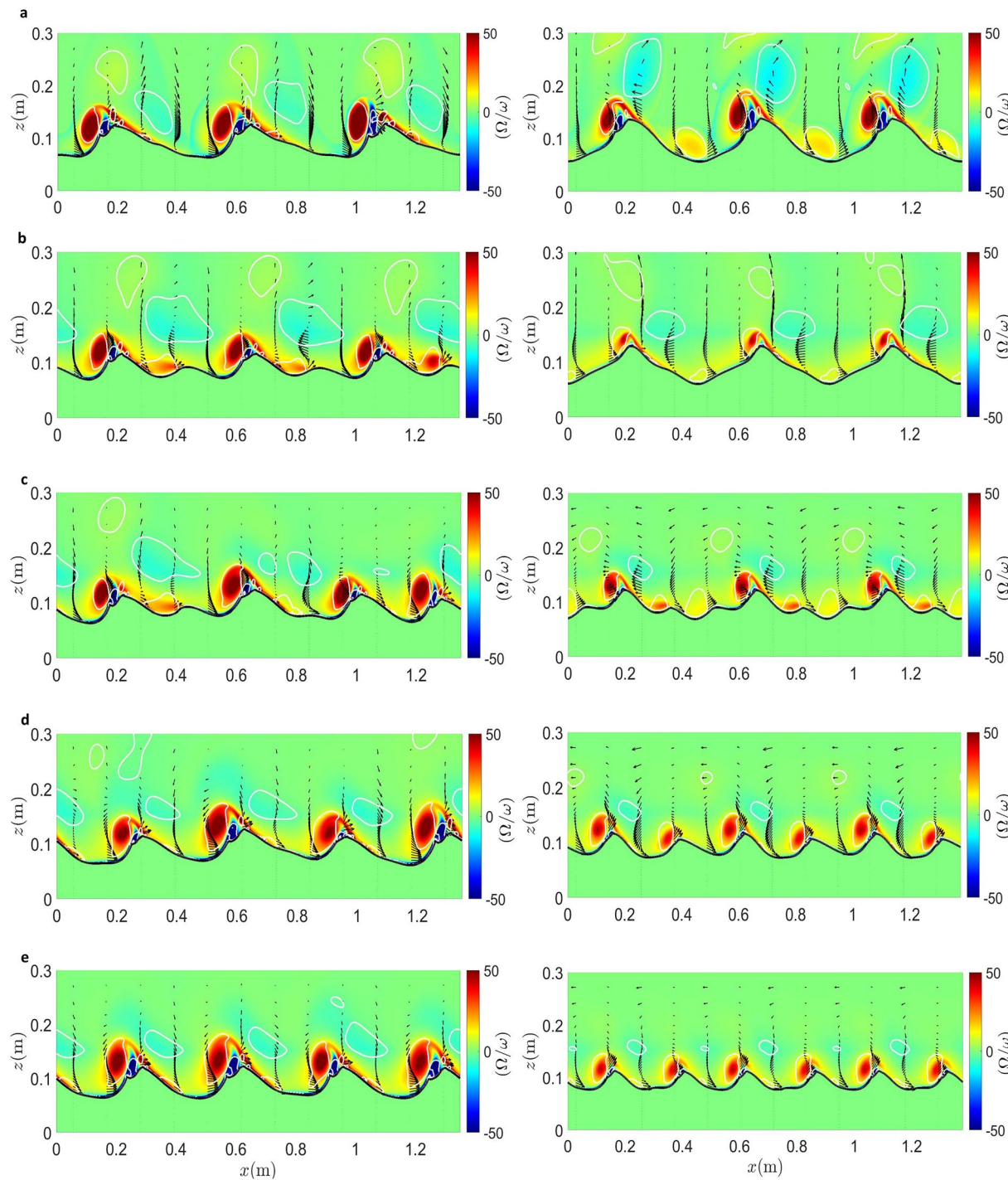


Figure 12. Snapshots of normalized vorticity field (color contour) for Case 2b (left panels) and Case 3 (right panels) at the end of (a) second wave period ($t = 6$ s), (b) tenth wave period ($t = 30$ s), (c) 30th wave period ($t = 90$ s), (d) 40th wave period ($t = 120$ s), and (e) 80th wave period ($t = 240$ s). The black contour shows the bed profile defined as the contour of volumetric concentration $\phi = 0.57$.

and 11d) to form a new ripple. The split and merge of smaller ripples are more dominated by the near-bed load (left panel of Figures 11b–11d).

To better illustrate the mechanisms forcing the evolution from larger ripples to smaller ripples through “protruding” (Case 2b) or “splitting” (Case 3), the normalized vorticity fields for Case 2b (left panels) and Case 3 (right panels) are presented in Figure 12. At the very early stage of the simulation, it is clear that

the vertical extent of the primary vortices on the offshore ripple flanks in Case 2b is larger than the ripple height, while in Case 3 it is only about half of the ripple height (Figure 12a). Although the vertical extent of the primary vortices in Case 2b is larger than the ripple height, due to the short flow period compared to Case 1 (but having the same wave orbital length), their sizes are limited horizontally (in the x -direction) and the vortex length is about 70% of the half ripple length ($\lambda / 2$). Because the vortex length cannot reach the trough of the initial ripples, the shorter vortices cause the formation of the smaller ripples in between the two initial larger ripples (i.e., protruding, see the left panel in Figure 12b). On the other hand, the primary vortices in Case 3 are both shorter than the ripple height and horizontally limited to the ripple flank due to smaller wave orbital length comparing to that of Case 1 and Case 2b and also smaller orbital velocity amplitude comparing to that of Case 2b. Therefore, the smaller ripples are carved by these vortices on the ripple flanks (splitting, see the right panel in Figure 12b). In Case 2b, the strong velocity and suspended load encourage protruding of new small ripples in-between two larger ripples and the subsequent merging and sliding of smaller ripples into the larger ones (left panels in Figures 12c and 12d) before arriving at the equilibrium state. Moreover, the equilibrium state is established when the vortices can reach the ripple trough (see the left panel in Figure 12e). In Case 3, the much smaller vortices directly split the initial large ripples into smaller ones and the two lateral smaller ripples merge with the adjacent small ripples (right panels of Figures 12c and 12d). At the equilibrium, the ripple length is adjusted such that the vortices also reach about half the equilibrium ripple length (see the right panel in Figure 12e).

The above comparison shows that not only the intensity of the vortices is important for the ripple geometry and evolution, but the size of the vortices also controls the ripple evolution and equilibrium geometry, especially the ripple length. As the vortex size is a function of both the flow intensity and the period, it supports the fact that the wave period plays an important role in ripple geometry formation and evolution. Earlier work quantifying ripple length using only the wave orbital length must assume a direct correlation between vortex length and wave orbital length. Simulation results presented here clearly show that although Case 1 and Case 2 have the same orbital excursion length, the vortex length in Case 2 with a shorter wave period is shorter than that in Case 1. Hence, this assumption may be too simplistic, especially for describing suborbital ripples. The orbital length can be used to parameterize the vortex length provided that there is enough time for the vortex to develop. When the wave period is short, this assumption may not be appropriate.

In Case 4, the initial small orbital ripples (the final ripple profile of Case 3) evolve into longer suborbital ripples due to an increase of oscillatory velocity amplitude (and hence orbital length). The interactions between the six initial smaller ripples with the larger vortices (the vortex length extends to the neighboring ripple flank, see right panel of Figure 13a), produced by the flow with larger orbital excursion length and velocity, cause the ripple flattening located at $x = 0.7$ m (see Figure 13b). Later, the large vortices (relative to the ripple length) above the ripples located at $x = 0.2$ m and $x = 0.5$ m cause these two ripples to slide away from each other (see Figure 13c). Meanwhile, two ripples initially located at $x = 1.1$ m and $x = 1.3$ m merge into each other by interacting with the large vortices above them. After adjusting their length by sliding away or toward each other, the vortices erode more sediment from the troughs toward the crests to grow the ripple height. At equilibrium, the vortices can reach about half of the ripple length (see Figure 13d). Simulation results presented here illustrate how large vortices can grow ripple size and reduce the number of ripples in the domain via flattening and merging. A similar mechanism has been investigated by Nienhuis et al. (2014) by analyzing a 2DV model's (Lattice Boltzmann model with Exner equation) vortex structures and associated bed shear stress distributions. They found that for slightly uneven spaced ripples, an increase of the orbital excursion length causes asymmetric vortex generation and shear stress distribution which drive the widely-spaced ripple pairs farther apart and closely-spaced pairs closer together. They proposed that this mechanism leads to the bulging pattern and formation of larger ripples.

In Case 5, orbital ripples (final ripple profile of Case 1) are washed out due to a significant increase of oscillatory velocity amplitude (Shields parameter exceeds 1.5) and the transition to sheet flow condition occurs. Snapshots of the different stages of the annihilation of the bed features are provided in Figure 14. In this case, the suspended load is dominant during the entire evolution. During the first wave period (0–5 s) the suspended load is much larger than the near-bed load (suspended load to near-bed load ratio of $R = 3.86$) as the steep ripples generate vortices driving a large amount of suspended load transport to rapidly flatten the ripples (Figure 14a). The flattening of the bed continues rapidly and soon no more vortices can be seen as

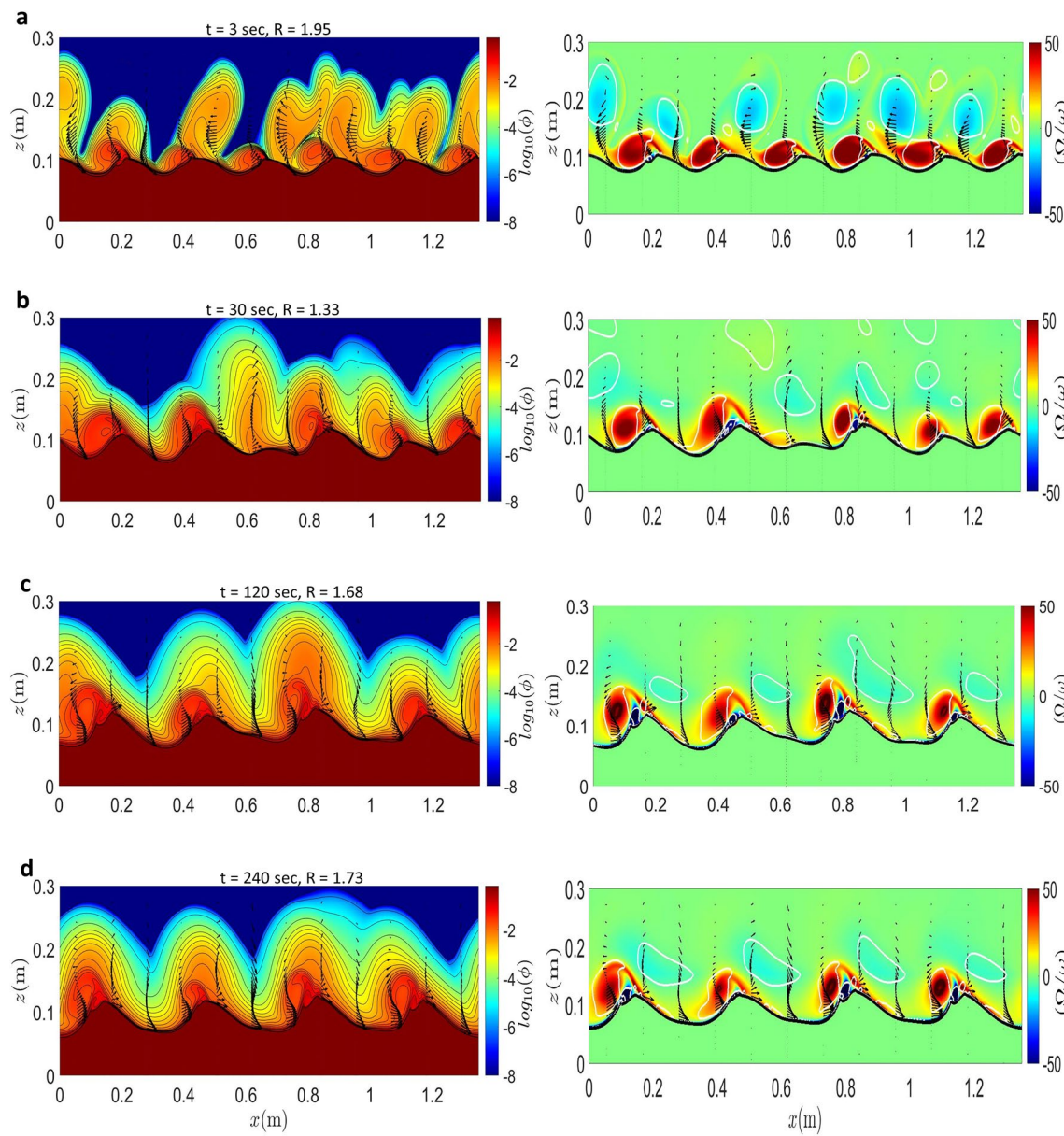


Figure 13. Snapshots of volumetric concentration field (left panels) and normalized vorticity field (right panels) for Case 4 at the end of (a) first wave period ($t = 3$ s), (b) tenth wave period ($t = 30$ s), (c) 40th wave period ($t = 120$ s), (d) 60th wave period ($t = 180$ s). The black contour in the right panels shows the bed profile defined as the contour of volumetric concentration $\phi = 0.57$.

the bed becomes relatively flat (see the right panels in Figure 14b). Between $t = 15$ – 30 s, the bed continues to adjust with the flow and becomes more flat (Figure 14c). Although the suspended load remains dominant at the later stage, the difference between the suspended load and near-bed load is not significant ($R = 1.08$).

As the ripples start to form from a nearly flat bed in Case 6, the near-bed load is always dominant, although the contribution from suspended load becomes increasingly important as the ripple steepness grows. Before $t = 60$ s, due to very small ripple steepness, the vortex-generation ejection process does not exist (see the right panel in Figure 15a). Vorticity is generated very near the bed due to boundary layer shear. Consequently, there is almost no suspended sediment in the domain with $R \approx 0$ (left panel in Figure 15a) and it is the near-bed load shaping the morphological evolution and generating many small bedforms of only a few centimeters in length. As time elapses, these small bedforms merge into each other. At $t = 60$ s, larger ripples (around 10 cm in length) can be seen (Figure 15b) and the vortex generation-ejection process begins to take

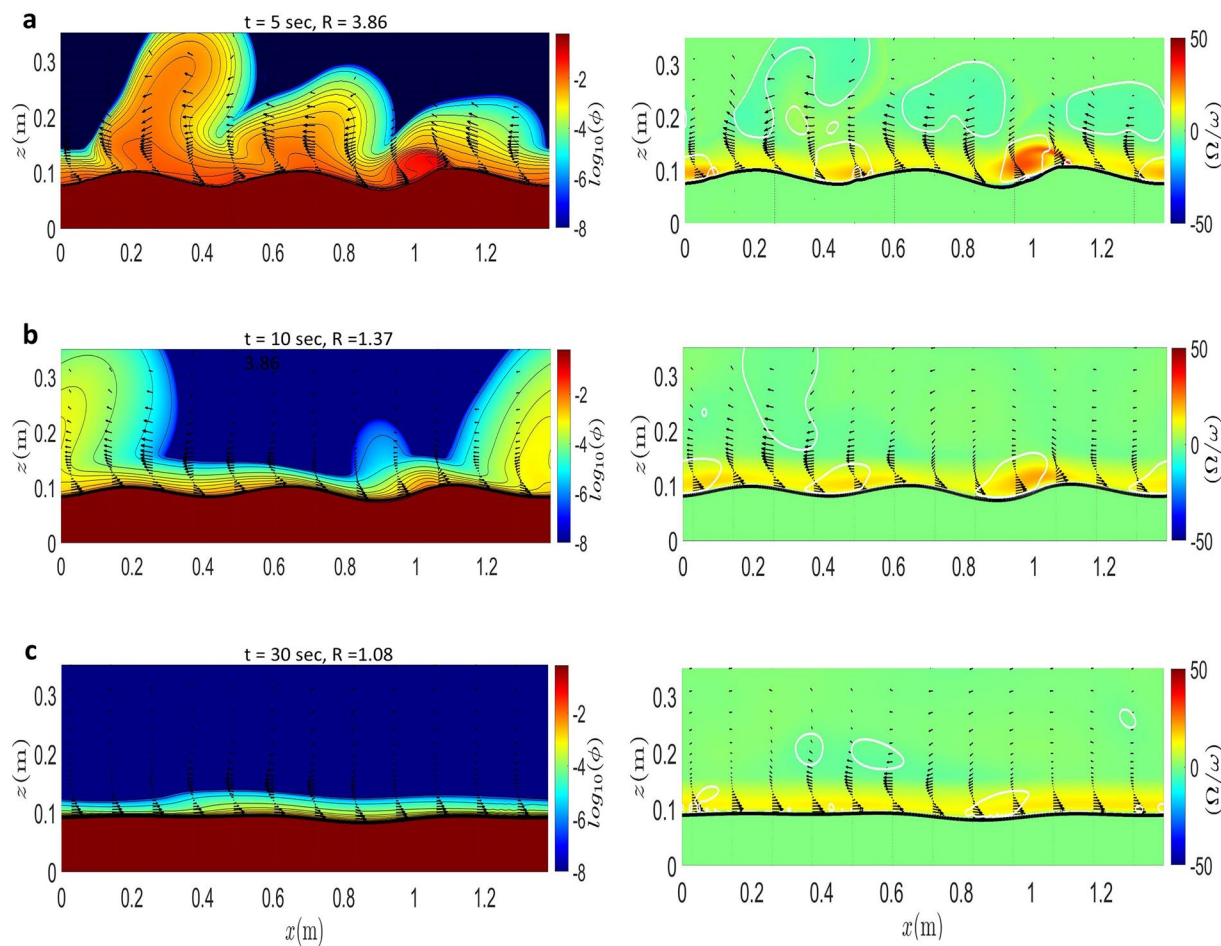


Figure 14. Snapshots of sediment concentration field (left panels) and normalized vorticity field (right panels) for Case 5 at end of the (a) first wave period ($t = 5 \text{ s}$), (b) second wave period ($t = 10 \text{ s}$), and (c) sixth wave period ($t = 30 \text{ s}$). The black contour in the right panels shows the bed profile defined as the contour of volumetric concentration $\phi = 0.57$.

place above the bedform located at $x = 0.62 \text{ m}$. The steepness of this particular bedform is $\eta / \lambda = 0.092$. Between $t = 60$ and 120 s the interaction between the bedforms and the vortices forces the smaller bedforms to further merge into each other and form even larger ripples above which an intense vortex generation-ejection process occurs (see Figure 15c). Meanwhile, more sediment is suspended into the water column by the vortices and the suspended load to near-bed load ratio increased to $R = 0.59$. Furthermore, between $t = 120$ and 180 s , due to the stronger and larger vortex generation, the smaller ripples located at $x = 0.38 \text{ m}$ and $x = 1.36 \text{ m}$ merge into the onshore flank of the adjacent (larger) ripples (see the right panel in Figure 15d) while R continues to grow gradually to 0.7. During the remainder of the simulation, the height and length of the ripples are continuously adjusted while the small ripple located at $x = 0.9 \text{ m}$ is almost washed away near the equilibrium state ($t = 300 \text{ s}$, see Figure 15e). At this stage, the transport rates reached the quasi-steady state with $R = 0.74$, the same as that in Case 1. The final ripple length and steepness are also similar to those obtained in Case 1.

In summary, the presence of vortices plays a key role in the ripple evolution and the equilibrium ripple geometry. The size of the vortices relative to the length scale of the bathymetry features controls the protruding, splitting, sliding, and merging behaviors during the ripple evolution. Moreover, the equilibrium ripple length is approximately two times the length of the primary vortex. This finding is consistent with the numerical study of Nienhuis et al. (2014).

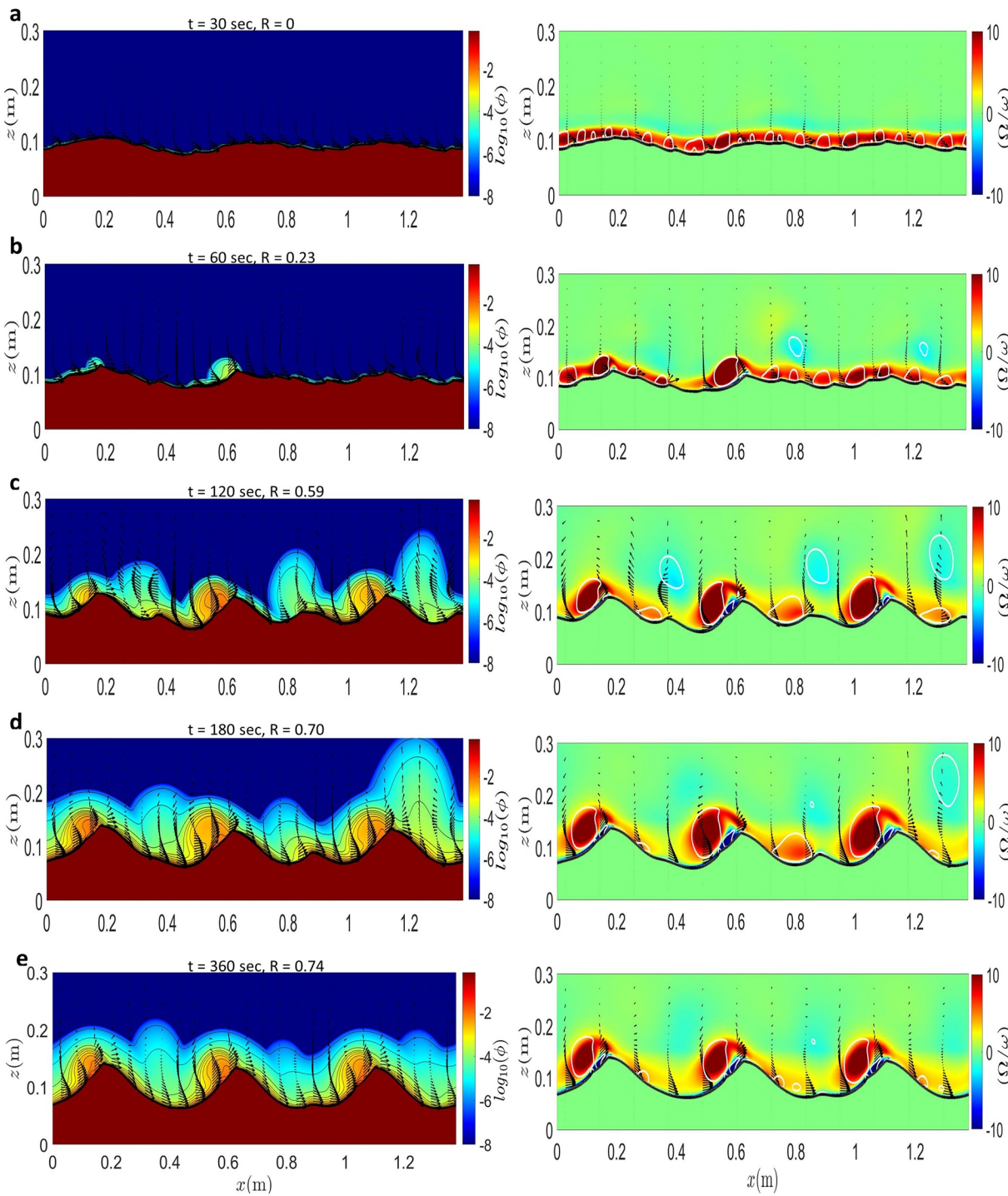


Figure 15. Snapshots of sediment concentration field (left panels) and normalized vorticity field (right panels) for Case 6 at the end of (a) sixth wave period ($t = 30 \text{ s}$), (b) 12th wave period ($t = 60 \text{ s}$), (c) 24th wave period ($t = 120 \text{ s}$), (d) 36th wave period ($t = 180 \text{ s}$), and (e) 72nd wave period ($t = 360 \text{ s}$). The black contour in the right panels shows the bed profile defined as the contour of volumetric concentration $\phi = 0.57$.

5. Conclusion

In this study, an Eulerian two-phase model for sediment transport, SedFoam has been utilized to investigate the effect of wave period on the ripple geometry and the ripple evolution in response to step-changes in the wave orbital motion. By keeping the same orbital excursion length in the oscillatory flow forcing between

two cases (i.e., Case 1 and Case2a), with different combinations of the wave period and the velocity amplitude, two different equilibrium ripples, the maximum orbital ripple (Case 1) and suborbital ripples (Case 2a), are obtained. These results confirm that solely using the (d_0 / D_{50}) is not adequate for predicting the ripple geometry. In general, for a given sediment size, modeled equilibrium ripple dimensions show a good agreement with those predictors that include the wave period T besides the non-dimensionalized orbital excursion length (d_0 / D_{50}), especially in the decaying (suborbital) regime. In particular, the model results agree very well with the O'Donoghue et al. (2006) predictor which combines T and d_0 / D_{50} in the form of mobility number (revised Nielsen (1981) predictor). Model results reveal that the main reason that wave period plays a role in the resulting ripple geometry is because wave period may limit the development time of the vortices and hence the dimension of the vortices, particularly the length, cannot be solely controlled by the orbital excursion length. Generally, model results indicate that the equilibrium ripple length is about twice the length of the primary vortices. When the primary vortex length is smaller than half of the ripple length, ripple splitting or protruding occurs and more ripples are formed. On the contrary, when the primary vortex length is larger than half of the ripple length, ripples can merge.

Although the dynamic coupling between the flow and the ripples is generally a three-dimension process (e.g., Hansen, van Hecke, Ellegaard, Andersen, Bohr, Haaning, & Sams, 2001), using the present two-dimensional two-phase formulation model can capture the major ripple evolution processes, including splitting, protruding, sliding, merging, transition to sheet flow, and reformation from a nearly flat bed. However, neglecting the three-dimensional process may have caused the more rapid ripple evolution predicted by the present two-dimensional simulations. To further resolve 3D intermittent patches during the ripple development, a 3D large-eddy simulation approach may be necessary. It is important in future works to utilize the model to simulate the three-dimensional ripple evolution dynamics and turbulence-sediment interaction.

Without the conventional bedload/suspended load assumption, the two-phase model results are used to reveal the contribution from near-bed load transport and suspended load transport for different ripple regimes. Model results indicate that in the orbital ripple regime, the near-bed load transport is dominant in the equilibrium state, while in the decaying regime (suborbital ripples and sheet flows) the suspended load is dominant. Model results are consistent with field observations (Traykovski et al, 1999; Wiberg & Harris, 1994). In this study, simulations are conducted only for one sediment size. It is well-known that sediment size plays an important role in ripple formation, geometry, and evolution. Hence further investigation with different sediment sizes is warranted.

Data Availability Statement

The source code and the case setup to reproduce the same results are publicly available via the sedFOAM's official website: <http://servforge.legi.grenoble-inp.fr/pub/soft-sedfoam/> or GitHub repository: <https://github.com/Ali-Salimi/sedfoam> (source code) and <https://github.com/Ali-Salimi/RippleEvol> (case setups).

Acknowledgments

This study is supported by National Science Foundation (OCE-1635151 and OCE-1924532) and Strategic Environmental Research and Development Program (MR20-1478). Numerical simulations presented in this study were carried out using the Caviness cluster at University of Delaware, and the Stampede2 cluster at the University of Texas at Austin via XSEDE. We like to thank Dr. Zhen Cheng for his contribution on the SedFoam source code development. We are also grateful to the developers involved in OpenFOAM, who are the foundation of the model presented in this paper.

References

- Bagnold, R. A., & Taylor, G. (1946). Motion of waves in shallow water. Interaction between waves and sand bottoms. *Proceedings of the Royal Society of London—Series A: Mathematical and Physical Sciences*, 187(1008), 1–18. <https://doi.org/10.1098/rspa.1946.0062>
- Blondeaux, P., & Vittori, G. (1991). Vorticity dynamics in an oscillatory flow over a rippled bed. *Journal of Fluid Mechanics*, 226(WW1), 257–289. <https://doi.org/10.1017/S0022112091002380>
- Chang, Y. S., & Hanes, D. M. (2004). Suspended sediment and hydrodynamics above mildly sloped long wave ripples. *Journal of Geophysical Research*, 109(C7), C07022. <https://doi.org/10.1029/2003JC001900>
- Chang, Y. S., & Scotti, A. (2003). Entrainment and suspension of sediments into a turbulent flow over ripples. *Journal of Turbulence*, 4. <https://doi.org/10.1088/1468-5248/4/1/019>
- Chauchat, J., Cheng, Z., Nagel, T., Bonamy, C., & Hsu, T.-J. (2017). SedFoam-2.0: A 3-D two-phase flow numerical model for sediment transport. *Geoscientific Model Development*, 10, 4367–4392. <https://doi.org/10.5194/gmd-10-4367-2017>
- Chauchat, J., & Médale, M. (2014). A three-dimensional numerical model for dense granular flows based on the $\mu(I)$ rheology. *Journal of Computational Physics*, 256, 696–712. <https://doi.org/10.1016/j.jcp.2013.09.004>
- Cheng, Z., Hsu, T. J., & Calantoni, J. (2017). SedFoam: A multi-dimensional Eulerian two-phase model for sediment transport and its application to momentary bed failure. *Coastal Engineering*, 119, 32–50. <https://doi.org/10.1016/j.coastaleng.2016.08.007>
- Chou, Y. J., & Fringer, O. B. (2010). A model for the simulation of coupled flow-bed form evolution in turbulent flows. *Journal of Geophysical Research*, 115(10), 1–20. <https://doi.org/10.1029/2010JC006103>
- Clifton, H. E. (1976). Wave-formed sedimentary structures: A conceptual model. In R. A. Davis Jr. & R. L. Ethington (Eds.), *Beach and nearshore sedimentation, Special Publication* (Vol. 24, pp. 126–148). Society for Sediment Geology.

- Crawford, A. M., & Hay, A. E. (2001). Linear transition ripple migration and wave orbital velocity skewness: Observations. *Journal of Geophysical Research*, 106(C7), 14113–14128. <https://doi.org/10.1029/2000JC000612>
- Dimas, A. A., & Leftheriotis, G. A. (2019). Mobility parameter and sand grain size effect on sediment transport over vortex ripples in the orbital regime. *Journal of Geophysical Research: Earth Surface*, 124(1), 2–20. <https://doi.org/10.1029/2018JF004741>
- Dohmen-Janssen, C. M., & Hanes, D. M. (2002). Sheet flow dynamics under monochromatic nonbreaking waves. *Journal of Geophysical Research*, 107(C10), 3149. <https://doi.org/10.1029/2001JC001045>
- Doucette, J. S., & O'Donoghue, T. (2006). Response of sand ripples to change in oscillatory flow. *Sedimentology*, 53(3), 581–596. <https://doi.org/10.1111/j.1365-3091.2006.00774.x>
- Evans, O. F. (1943). Effect of change of wave size on the size and shape of ripple marks. *Journal of Sedimentary Research*, 13 (1): 35–39. <https://doi.org/10.1306/D4269189-2B26-11D7-8648000102C1865D>
- Grant, W. D., & Madsen, O. S. (1982). Movable bed roughness in unsteady oscillatory flow. *Journal of Geophysical Research*, 87(C1), 469–481. <https://doi.org/10.1029/JC087iC01p00469>
- Hansen, J. L., van Hecke, M., Ellegaard, C., Andersen, K. H., Bohr, T., Haaning, A., & Sams, T. (2001). Stability balloon for two-dimensional vortex ripple patterns. *Physical Review Letters*, 87(20), 204301. <https://doi.org/10.1103/PhysRevLett.87.204301>
- Hansen, J. L., van Hecke, M., Ellegaard, C., Andersen, K. H., Bohr, T., & Sams, T. (2001). Pattern formation: Instabilities in sand ripples. *Nature*, 410, 324. <https://doi.org/10.1038/35066631>
- Harris, J. C., & Grilli, S. T. (2014). Large eddy simulation of sediment transport over rippled beds. *Nonlinear Processes in Geophysics*, 21, 1169–1184. <https://doi.org/10.5194/npg-21-1169-2014>
- Hay, A. E., & Mudge, T. (2005). Principal bed states during SandyDuck97: Occurrence, spectral anisotropy, and the bed state storm cycle. *Journal of Geophysical Research: Oceans*, 110(3), 1–18. <https://doi.org/10.1029/2004JC002451>
- Johnson, P. C., Nott, P., & Jackson, R. (1990). Frictional-collisional equations of motion for particulate flows and their application to chutes. *Journal of Fluid Mechanics*, 210, 501–535. <https://doi.org/10.1017/S0022112090001380>
- Lanckriet, T., & Puleo, J. A. (2015). A semianalytical model for sheet flow layer thickness with application to the swash zone. *Journal of Geophysical Research: Oceans*, 120, 1333–1352. <https://doi.org/10.1002/2014JC010378>
- Longuet-Higgins, M. (1981). Oscillating flow over steep sand ripples. *Journal of Fluid Mechanics*, 107, 1–35. <https://doi.org/10.1017/S0022112081001651>
- Malarkey, J., & Davies, A. G. (2003). A non-iterative procedure for the Wiberg and Harris (1994) oscillatory sand ripple predictor. *The Journal of Coastal Research*, 19(3), 738–739.
- Marie, V., Bonneton, P., Foster, D. L., & Ardhuin, F. (2008). Modeling of vortex ripple morphodynamics. *Journal of Geophysical Research: Oceans*, 113(9), 1–15. <https://doi.org/10.1029/2007JC004659>
- Miller, M. C., & Komar, P. D. (1980). Oscillation sand ripples generated by laboratory apparatus. *Journal of Sedimentary Petrology*, 50(1), 173–182. <https://doi.org/10.1306/212f799b-2b24-11d7-8648000102c1865d>
- Mogridge, G. R., Davies, M. H., & Willis, D. H. (1994). Geometry prediction for wave-generated bedforms. *Coastal Engineering*, 22(3–4), 255–286. [https://doi.org/10.1016/0378-3839\(94\)90039-6](https://doi.org/10.1016/0378-3839(94)90039-6)
- Mogridge, G. R., & Kamphuis, J. W. (1972). Experiments on bed form generation by wave action. In *Proceedings of 13th Conference on Coastal Engineering, Vancouver, July 10–14, 1972* (Vol. 2, pp. 1123–1142). <https://doi.org/10.1061/978087260490.063>
- Nelson, T., Voulgaris, G., & Traykovski, P. (2013). Predicting wave-induced ripple equilibrium geometry. *Journal of Geophysical Research: Oceans*, 118(6), 3202–3220. <https://doi.org/10.1002/jgrc.20241>
- Nielsen, P. (1981). Dynamics and geometry of wave-generated ripples. *Journal of Geophysical Research*, 86(1), 6467–6472. <https://doi.org/10.1029/jc086ic07p06467>
- Nielsen, P. (1992). *Coastal bottom boundary layers and sediment transport*. World Scientific.
- Nienhuis, J. H., Perron, J. T., Kao, J. C. T., & Myrow, P. M. (2014). Wavelength selection and symmetry breaking in orbital wave ripples. *Journal of Geophysical Research: Earth Surface*, 119(10), 2239–2257. <https://doi.org/10.1002/2014JF003158>
- O'Donoghue, T., & Clubb, G. S. (2001). Sand ripples generated by regular oscillatory flow. *Coastal Engineering*, 44(2), 101–115. [https://doi.org/10.1016/S0378-3839\(01\)00025-4](https://doi.org/10.1016/S0378-3839(01)00025-4)
- O'Donoghue, T., Doucette, J. S., van der Werf, J. J., & Ribberink, J. S. (2006). The dimensions of sand ripples in full-scale oscillatory flows. *Coastal Engineering*, 53(12), 997–1012. <https://doi.org/10.1016/j.coastaleng.2006.06.008>
- O'Donoghue, T., & Wright, S. (2004). Flow tunnel measurements of velocities and sand flux in oscillatory sheet flow for well-sorted and graded sands. *Coastal Engineering*, 51(11–12), 1163–1184. <https://doi.org/10.1016/j.coastaleng.2004.08.001>
- Önder, A., & Yuan, J. (2019). Turbulent dynamics of sinusoidal oscillatory flow over a wavy bottom. *Journal of Fluid Mechanics*, 858, 264–314. <https://doi.org/10.1017/jfm.2018.754>
- Pedocchi, F., & García, M. H. (2009). Ripple morphology under oscillatory flow: 1. Prediction. *Journal of Geophysical Research*, 114(12), 1–16. <https://doi.org/10.1029/2009JC005354>
- Penko, A. M., Calantoni, J., Rodriguez-Abudo, S., Foster, D. L., & Slinn, D. N. (2013). Three-dimensional mixture simulations of flow over dynamic rippled beds. *Journal of Geophysical Research: Oceans*, 118, 1543–1555. <https://doi.org/10.1002/jgrc.20120>
- Penko, A. M., Slinn, D. N., & Calantoni, J. (2011). Model for mixture theory simulation of vortex sand ripple dynamics. *Journal of Waterway, Port, Coastal, and Ocean Engineering*, 137(5), 225–233. [https://doi.org/10.1061/\(ASCE\)WW.1943-5460.0000084](https://doi.org/10.1061/(ASCE)WW.1943-5460.0000084)
- Perron, J. T., Myrow, P. M., Huppert, K. L., Koss, A. R., & Wickert, A. D. (2018). Ancient record of changing flows from wave ripple defects. *Geology*, 46(10), 875–878. <https://doi.org/10.1130/G45463.1>
- Ribberink, J. S., van der Werf, J. J., O'Donoghue, T., & Hassan, W. N. M. (2008). Sand motion induced by oscillatory flows: Sheet flow and vortex ripples. *Journal of Turbulence*, 9, 1–32. <https://doi.org/10.1080/14685240802220009>
- Salimi-Tarazouj, A., Hsu, T.-J., Traykovski, P., Cheng, Z., & Chauchat, J. (2021). A numerical study of onshore ripple migration using a Eulerian two-phase model. *Journal of Geophysical Research: Oceans*, 126, e2020JC016773. <https://doi.org/10.1029/2020JC016773>
- Scandura, P., Vittori, G., & Blondeaux, P. (2000). Three-dimensional oscillatory flow over steep ripples. *Journal of Fluid Mechanics*, 412, 355–378. <https://doi.org/10.1017/S0022112000008430>
- Schaeffer, D. G. (1987). Instability in the evolution equations describing the incompressible granular flow. *Journal of Differential Equations*, 66(1), 19–50. [https://doi.org/10.1016/0022-0833\(87\)90038-6](https://doi.org/10.1016/0022-0833(87)90038-6)
- Sekiguchi, T., & Sunamura, T. (2004). A laboratory study of formative conditions for characteristic ripple patterns associated with a change in wave conditions. *Earth Surface Processes and Landforms*, 29(11), 1431–1435. <https://doi.org/10.1002/esp.1139>
- Soulsby, R. L., & Whitehouse, R. J. S. (2005). *Prediction of ripple properties in shelf seas* (Technical Report). U.S. Office of Naval Research.
- Swart (1974). *Offshore sediment transport and equilibrium beach profiles* (Publication No. 131). Delft Hydraulics Laboratory.

- Testik, F. Y., Voropayev, S. I., & Fernando, H. J. S. (2005). Adjustment of sand ripples under changing water waves. *Physics of Fluids*, 17(7), 1–8. <https://doi.org/10.1063/1.1946768>
- Traykovski, P. (2007). Observations of wave orbital scale ripples and a nonequilibrium time-dependent model. *Journal of Geophysical Research*, 112(6), 1–19. <https://doi.org/10.1029/2006JC003811>
- Traykovski, P., Hay, A. E., Irish, J. D., & Lynch, J. F. (1999). Geometry, migration, and evolution of wave orbital ripples at LEO-15. *Journal of Geophysical Research*, 104(C1), 1505–1524. <https://doi.org/10.1029/1998JC900026>
- van der Werf, J. J., Doucette, J. S., O'Donoghue, T., & Ribberink, J. S. (2007). Detailed measurements of velocities and suspended sand concentrations over full-scale ripples in regular oscillatory flow. *Journal of Geophysical Research*, 112(2), 1–18. <https://doi.org/10.1029/2006JF000614>
- van der Werf, J. J., Magar, V., Malarkey, J., Guizien, K., & O'Donoghue, T. (2008). 2DV modeling of sediment transport processes over full-scale ripples in regular asymmetric oscillatory flow. *Continental Shelf Research*, 28(8), 1040–1056. <https://doi.org/10.1016/j.csres.2008.02.007>
- van der Werf, J. J., Ribberink, J. S., O'Donoghue, T., & Doucette, J. S. (2006). Modeling and measurement of sand transport processes over full-scale ripples in oscillatory flow. *Coastal Engineering*, 53(8), 657–673. <https://doi.org/10.1016/j.coastaleng.2006.02.002>
- Voropayev, S. I., McEachern, G. B., Boyer, D. L., & Fernando, H. J. S. (1999). Dynamics of sand ripples and burial/scouring of cobbles in oscillatory flow. *Applied Ocean Research*, 21(5), 249–261. [https://doi.org/10.1016/S0141-1187\(99\)00015-2](https://doi.org/10.1016/S0141-1187(99)00015-2)
- Weller, H. G., Tabor, G., Jasak, H., & Fureby, C. (1998). A tensorial approach to computational continuum mechanics using object-oriented techniques. *Computers in Physics*, 12(6), 620. <https://doi.org/10.1063/1.168744>
- Wiberg, P. L., & Harris, C. K. (1994). Ripple geometry in wave-dominated environments. *Journal of Geophysical Research*, 99(C1), 775–789. <https://doi.org/10.1029/93JC02726>
- Zedler, E. A., & Street, R. L. (2006). Sediment transport over ripples in oscillatory flow. *Journal of Hydraulic Engineering*, 132(2), 180–193. [https://doi.org/10.1061/\(asce\)0733-9429\(2006\)132:2\(180\)](https://doi.org/10.1061/(asce)0733-9429(2006)132:2(180))
- Zlatanović, S., Fabian, J., Mendoza-Lera, C., Woodward, K. B., Premke, K., & Mutz, M. (2017). Periodic sediment shift in migrating ripples influences benthic microbial activity. *Water Resources Research*, 53(6), 4741–4755. <https://doi.org/10.1002/2017WR020656>